



**QUEEN'S  
UNIVERSITY  
BELFAST**

## Ultrahigh-current-density niobium disulfide catalysts for hydrogen evolution

Yang, J., Mohmad, A. R., Wang, Y., Fullon, R., Song, X., Zhao, F., Bozkurt, I., Augustin, M., Santos, E. J. G., Shin, H. S., Zhang, W., Voiry, D., Jeong, H. Y., & Chhowalla, M. (2019). Ultrahigh-current-density niobium disulfide catalysts for hydrogen evolution. *Nature Materials*, 18(2019), 1309. <https://doi.org/10.1038/s41563-019-0463-8>

**Published in:**  
Nature Materials

**Document Version:**  
Peer reviewed version

**Queen's University Belfast - Research Portal:**  
[Link to publication record in Queen's University Belfast Research Portal](#)

**Publisher rights**  
Copyright 2019 Nature Research. This work is made available online in accordance with the publisher's policies. Please refer to any applicable terms of use of the publisher.

**General rights**  
Copyright for the publications made accessible via the Queen's University Belfast Research Portal is retained by the author(s) and / or other copyright owners and it is a condition of accessing these publications that users recognise and abide by the legal requirements associated with these rights.

**Take down policy**  
The Research Portal is Queen's institutional repository that provides access to Queen's research output. Every effort has been made to ensure that content in the Research Portal does not infringe any person's rights, or applicable UK laws. If you discover content in the Research Portal that you believe breaches copyright or violates any law, please contact [openaccess@qub.ac.uk](mailto:openaccess@qub.ac.uk).

# 1            **Ultrahigh current density niobium disulfide catalysts for hydrogen evolution**

2    Jieun Yang<sup>1,†</sup>, Abdul Rahman Mohmad<sup>2,†</sup>, Yan Wang<sup>1</sup>, Raymond Fullon<sup>1</sup>, Xiuju Song<sup>1,3</sup>, Fang  
3    Zhao<sup>4</sup>, Ibrahim Bozkurt<sup>1</sup>, Mathias Augustin<sup>5</sup>, Elton J. G. Santos<sup>5\*</sup>, Hyeon Suk Shin<sup>6</sup>, Damien  
4    Voiry<sup>7</sup>, Hu Young Jeong<sup>8,\*</sup>, Manish Chhowalla<sup>1,3\*#</sup>

## 5    **Affiliations:**

6    <sup>1</sup>*Materials Science and Engineering, Rutgers University, 607 Taylor Road, Piscataway, New*  
7    *Jersey 08854, USA.*

8    <sup>#</sup>*Current Address: Department of Materials Science & Metallurgy, University of Cambridge, 27*  
9    *Charles Babbage Road, Cambridge CB3 0FS, UK.*

10    <sup>2</sup>*Institute of Microengineering and Nanoelectronics, National University of Malaysia (UKM),*  
11    *43600 Bangi, Selangor, Malaysia*

12    <sup>3</sup>*SZU-RUT Collaborative Innovation Center for Optoelectronic Science & Technology,*  
13    *International Collaborative Laboratory of 2D Materials for Optoelectronics Science and*  
14    *Technology of Ministry of Education, College of Optoelectronic Engineering, Shenzhen*  
15    *University, Shenzhen 518060, China.*

16    <sup>4</sup>*Department of Physics, Princeton University, Jadwin Hall, Princeton New Jersey 08544, USA*

17    <sup>5</sup>*School of Mathematics and Physics, Queen's University Belfast, BT71NN, United Kingdom*

18    <sup>6</sup>*Department of Chemistry and Department of Energy Engineering, Low-Dimensional Carbon*  
19    *Materials Center, Ulsan National Institute of Science and Technology (UNIST), UNIST-gil 50,*  
20    *Ulsan 44919, Republic of Korea*

21    <sup>7</sup>*Institut Européen des Membranes (I.E.M.), University of Montpellier, Place Eugène Bataillon,*  
22    *34095 Montpellier, France*

23    <sup>8</sup>*UNIST Central Research Facilities (UCRF) and School of Materials Science and Engineering,*  
24    *UNIST, Ulsan 689-798, Republic of Korea*

25    \*Correspondence to: [e.santos@qub.ac.uk](mailto:e.santos@qub.ac.uk), [hulex@unist.ac.kr](mailto:hulex@unist.ac.kr) and [mc209@cam.ac.uk](mailto:mc209@cam.ac.uk)

26    <sup>†</sup> *These authors contributed equally to this work.*

27  
28  
29  
30  
31  
32  
33  
34  
35

36  
37 **Two-dimensional metallic transition metal dichalcogenides (2D TMDs) such as 1T phases**  
38 **of MoS<sub>2</sub><sup>1,2</sup> and WS<sub>2</sub><sup>3</sup>, NbS<sub>2</sub><sup>4</sup>, TaS<sub>2</sub><sup>4-6</sup> and VS<sub>2</sub><sup>7,8</sup> have been studied as potentially**  
39 **inexpensive and earth abundant electrocatalysts for the hydrogen evolution reaction**  
40 **(HER). The performance of HER catalysts is typically evaluated in terms of overpotential**  
41 **at which the reaction starts and the Tafel slope – a measure of the over-potential required**  
42 **to increase a reaction by a factor of 10. The overpotential and Tafel slope values of metallic**  
43 **phases and edges<sup>9</sup> of 2D TMDs approach those of Pt nanoparticles – the best HER catalyst.**  
44 **However, despite substantial progress the overall current density of 2D TMD catalysts**  
45 **remains orders of magnitude lower (~ 10 – 100 mA-cm<sup>-2</sup>) than industrial Pt and Ir**  
46 **electrolyzers (> 1,000 mA-cm<sup>-2</sup>)<sup>10,11</sup>. Here, we report the synthesis of three dimensional**  
47 **(3D) niobium disulfide (Nb<sub>1+x</sub>S<sub>2</sub> where *x* is ~ 0.35)<sup>12</sup> as a HER catalyst that is capable of**  
48 **evolving hydrogen at current densities of > 5,000 mA-cm<sup>-2</sup> at an overpotential of ~420 mV**  
49 ***versus* reversible hydrogen electrode (RHE). We find the exchange current density at 0 V**  
50 **for 2H phase Nb<sub>1.35</sub>S<sub>2</sub> catalysts to be ~ 0.8 mA-cm<sup>-2</sup> (comparable to that of noble metals),**  
51 **corresponding to a turnover frequency of ~ 0.2 s<sup>-1</sup>. We demonstrate a proof of concept**  
52 **electrolyzer based on 2H Nb<sub>1.35</sub>S<sub>2</sub> cathode that is capable of generating current densities of**  
53 **1000 mA-cm<sup>-2</sup>. Our theoretical results reveal that the Nb<sub>1.35</sub>S<sub>2</sub> with Nb terminated surface**  
54 **has free energy for hydrogen adsorption that is close to thermoneutral, facilitating HER.**  
55 **The Nb<sub>1+x</sub>S<sub>2</sub> could therefore be a viable non-precious metal catalyst for practical**  
56 **electrolyzers used to generate hydrogen.**

57  
58 Ultra-thin layers of TMD catalysts exhibit improved electrocatalytic performance due to efficient  
59 charge injection and transfer to active sites<sup>13,14</sup>. Increasing the conductivity via engineering of  
60 metallic phases<sup>2,15,16</sup> and edges<sup>14,17-19</sup> also leads to substantial improvement in catalytic  
61 properties. To this end, metallic 1T phase of semiconducting MoS<sub>2</sub> induced by lithium  
62 chemistry<sup>1,2,20</sup> has been widely studied for HER catalysis. Recently, multi-layers of thin metallic  
63 TMDs such as NbS<sub>2</sub><sup>4</sup>, TaS<sub>2</sub><sup>5</sup>, and VS<sub>2</sub><sup>7</sup> have also been studied for HER. The key advantage of  
64 metallic TMDs according to theory is that the entire basal plane is catalytically active for the  
65 HER<sup>4,21,22</sup>, unlike in semiconducting MoS<sub>2</sub> where only the metallic edges are active<sup>9</sup>. However,  
66 in contrast with noble metal catalysts such as Pt nanoparticles, the electronic structure of

67 atomically thin materials is strongly influenced by local electrochemical reactions. For example,  
68 in the case of metallic 1T phase MoS<sub>2</sub>, the adsorption of protons on the surface – the first step in  
69 the HER – can dramatically reduce the conductivity of the 2D nanosheets<sup>21</sup>, which can slow  
70 down the reaction kinetics and reduce the overall current density. Thus, a fine balance must be  
71 achieved between reducing the thickness of catalysts and maintaining metallic nature of 2D  
72 materials to maximize catalytic performance.

73  
74 NbS<sub>2</sub> is a layered material that can exist in the hexagonal (2H phase) or rhombohedral (3R)  
75 crystal configurations (see Extended Data Fig. 1a,b,d,e). Metallic 2H phase NbS<sub>2</sub> has been  
76 predicted to be one of the most efficient electrocatalysts for the HER among the different types  
77 of TMDs<sup>22</sup>. In addition to the 2H and 3R phases, an unexplored non-layered 3D polytype with  
78 Nb<sub>1+x</sub>S<sub>2</sub> (where  $x$  is  $\sim 0.35$ ) stoichiometry, first synthesized in 1960 (Ref<sup>12</sup>), consisting of excess  
79 niobium strongly bonded to NbS<sub>2</sub> layers is also stable (see Extended Data Fig. 1c,f). We find that  
80 the exceed Nb Nb<sub>1+x</sub>S<sub>2</sub> phase can be synthesized by adjusting the CVD growth parameters (see  
81 Methods). Atomic force microscopy (AFM) image of typical Nb<sub>1+x</sub>S<sub>2</sub> crystals synthesized by  
82 chemical vapor deposition is shown in Figure 1a. Films of varying thicknesses ranging from 2  
83 nm to 50 nm with lateral dimensions of  $\sim 0.5 - 1 \mu\text{m}$  were realized by CVD on substrates such as  
84 SiO<sub>2</sub> and glassy carbon. We find that the phase of NbS<sub>2</sub> is dependent on the thickness of the  
85 material (Extended Data Fig. 2a-c). The electron diffraction patterns corresponding to the phases  
86 as a function of thickness are provided in Extended Data Fig. 2d,e. In particular, 2H – Nb<sub>1+x</sub>S<sub>2</sub> is  
87 predominantly observed in crystals with thickness of less than  $\sim 20$  nm while the 3R phase is  
88 primarily stable for thicker samples. High-resolution annular dark field (ADF) cross-sectional  
89 STEM images of Nb<sub>1+x</sub>S<sub>2</sub> clearly reveal Nb in both 2H phase (Figure 1b) and the 3R phase  
90 (Figure 1c). The  $d_{(0002)}$  spacing for the 2H excess Nb phase ( $6.35 \text{ \AA}$ ,  $c = 12.60 \text{ \AA}$ ) was found to  
91 be close to the theoretical value of the Nb<sub>1.35</sub>S<sub>2</sub> composition. The lower contrast in ADF image of  
92 the intercalated Nb planes is attributed to partial occupation of these sites (occupancy of 0.35 in  
93 excess layers versus 1 in the NbS<sub>2</sub> 2H and 3R layers). Additional evidence for intercalated Nb  
94 atoms in the form of Z contrast scans of atoms and chemical analyses are provided in Extended  
95 Data Fig. 3a,b. X-ray diffraction (XRD) spectrum shown in Extended Data Fig. 3c provides  
96 additional evidence for the intercalated hexagonal phase of NbS<sub>2</sub>. Direct synthesis of intercalated  
97 layered compounds with CVD is highly beneficial for preserving the high quality of the material.

98 That is, intercalation involving wet chemistry can lead to undesirable local reactions and  
99 deterioration of the material properties.

100  
101 The catalytic properties of NbS<sub>2</sub> and other metallic TMDs such as TaS<sub>2</sub> and VS<sub>2</sub> have been  
102 measured in several studies<sup>4,5,7</sup>. The results generally reveal Tafel slopes of ~ 40 mV-dec<sup>-1</sup> and  
103 low overpotential values of tens of millivolts *vs* RHE. For comparison, the overpotential at which  
104 HER proceeds for Pt nanoparticles is 0 V *vs* RHE with a corresponding Tafel slope of ~ 30 mV-  
105 dec<sup>-1</sup>. Despite the promising overpotentials and Tafel slopes achieved with metallic TMD  
106 catalysts, the maximum reported current density value has remained around ~ 100 mA-cm<sup>-2</sup>. The  
107 current density is limited by the multiple layers of metallic TMDs. That is, in contrast to phase  
108 transformed 1T metallic MoS<sub>2</sub> nanosheets that are single layered, it is generally challenging to  
109 synthesize or exfoliate metal TMDs down to the monolayer. Thus, most metallic NbS<sub>2</sub> and TaS<sub>2</sub>  
110 catalysts are multilayered and therefore electrons injected from the glassy carbon support must  
111 overcome the van der Waals gaps between the layers to reach the active sites on the surface. This  
112 increases the charge transfer resistance and thus the catalytic activity has been demonstrated to  
113 be inversely related to the number of layers in TMDs<sup>23</sup>. In the case of single layers, while the  
114 charge transfer kinetics are improved, the current carrying capability is lower and therefore the  
115 overall current density that can be achieved is also lower. Furthermore, the recombination of  
116 protons with free electrons on the surface of the single layer catalysts (the first step of the  
117 reaction) decreases the concentration of free carriers and therefore the conductivity<sup>21</sup>, reducing  
118 the kinetics of the HER and lowering the current density.

119  
120 We have tested the catalytic performance of metallic 2H Nb<sub>1.35</sub>S<sub>2</sub> with improved conductivity via  
121 elimination of van der Waals gaps between layers. This Nb<sub>1.35</sub>S<sub>2</sub> phase for HER was directly  
122 grown at 1273 K (CVD parameters are described in Methods) on high-quality glassy carbon  
123 electrodes. The HER was measured in 0.5M H<sub>2</sub>SO<sub>4</sub> electrolyte (see Methods for detailed  
124 description of measurements). The current density as a function of potential (*vs* RHE) from 2H,  
125 3R NbS<sub>2</sub>, and excess Nb 2H phase Nb<sub>1.35</sub>S<sub>2</sub> along with those from 3R Nb<sub>1.35</sub>S<sub>2</sub>, 2H and 1T  
126 phases of MoS<sub>2</sub> and WS<sub>2</sub> ref<sup>3</sup>, 2H and 3R NbS<sub>2</sub>, and Pt for comparison are shown in Figure 2a.  
127 It can be clearly seen from the polarization curves that the current density for the 2H Nb<sub>1.35</sub>S<sub>2</sub> is  
128 exceptionally large, reaching 1000 mA-cm<sup>-2</sup> at ~ 370 mV and 5,000 mA-cm<sup>-2</sup> at ~ 420 mV. This

129 current density is obtained from careful analyses of the catalytic active area. We have examined  
130 of numerous scanning electron microscope images to determine the areal coverage of catalyst  
131 material on the glassy carbon surface. We found that  $20\% \pm 5\%$  of the electrode surface is  
132 covered by the catalyst particles, see Extended Data Fig. 4. In addition to the areal coverage, we  
133 also carefully measured the electrochemical surface area (see Extended Data Fig. 5) to find the  
134 roughness factor ( $RF = 11 \pm 3$ ). Using this value, we were able to accurately determine the active  
135 area of the catalyst and use it to calculate the current density. To complement the current density  
136 measurements, we measured the actual amount of evolved hydrogen using a gas chromatograph  
137 (GC, Agilent 7890 B) equipped with molecular sieve  $5 \text{ \AA}$  capillary column and a thermal  
138 conductivity detector (TCD). The measurements were performed in a gas-tight 3-electrode cell.  
139 Ar gas was purged in the cell to remove air. The TCD cell was calibrated using known hydrogen  
140 amounts (5% and 10 %  $\text{H}_2$  balance Ar certified standard gas). The volume of hydrogen evolved  
141 by the  $2\text{H-Nb}_{1.35}\text{S}_2$  electrodes was measured at two overpotentials. We found that  $2\text{H-Nb}_{1.35}\text{S}_2$   
142 can evolve  $\text{H}_2$  up to  $150 \mu\text{mol}\cdot\text{h}^{-1}$  and  $300 \mu\text{mol}\cdot\text{h}^{-1}$  at 300mV and 400 mV, respectively. When  
143 normalizing the performance to the surface area, the rate of  $\text{H}_2$  evolution reaches  $\sim 30 \text{ L}\cdot\text{cm}^{-2}\cdot\text{h}^{-1}$   
144 equivalent to  $6 \text{ mmol}\cdot\text{h}^{-1}\cdot\text{cm}^{-2}$  at 400 mV. the Faradaic efficiency for the HER is typically 100%  
145 and therefore the current density is a direct indication of the amount of hydrogen evolved. Thus,  
146 careful measurement of the electrochemical surface area to obtain current density is a good  
147 indicator of catalyst performance. To confirm this, we measured the Faradaic efficiency using,  
148  $FE = \frac{2nF}{Q}$  where  $n$  is the moles of hydrogen measured from GC,  $F$  is the Faraday constant,  $Q$  is  
149 the charge obtained from measurements in Figure 2a of the MS ( $Q = I \times t$ , where  $I$  is the current  
150 and  $t$  is the time). The obtained efficiencies are 96% and 100% at 300 mV and 400 mV,  
151 respectively. Thus, the GC measurements confirm the electrochemical measurements and  
152 provide additional evidence for the high performance of  $2\text{H-Nb}_{1.35}\text{S}_2$ .

153  
154 It can be seen from Figure 2b, which provides an expanded view of the low overpotential region  
155 in Figure 2a, that the cathodic potential at which the HER starts is less than 100 mV  
156 (overpotential of  $< 150 \text{ mV}$ ) for the  $2\text{H Nb}_{1.35}\text{S}_2$  catalysts. The reaction for metallic  $2\text{H Nb}_{1.35}\text{S}_2$   
157 phase starts immediately upon application of the potential and proceeds slowly initially but as the  
158 potential is increased, it proceeds rapidly with very high current densities. The Tafel slopes  
159 shown in Figure 2c provide additional information about the rate limiting step in the catalytic

160 performance. Tafel slope values can vary from 30 mV-dec<sup>-1</sup> for Pt –indicating that HER is  
161 limited by the recombination of adsorbed hydrogens – to > 120 mV-dec<sup>-1</sup> where adsorption of  
162 protons limits the catalytic activity. It can be seen that the Tafel slope for 2H phase Nb<sub>1.35</sub>S<sub>2</sub>  
163 catalysts is 43 mV-dec<sup>-1</sup> (and ~ 38 mV-dec<sup>-1</sup> after *iR* correction) at low overpotentials (100 – 120  
164 mV), which is comparable to what has been measured for metallic 1T phase MoS<sub>2</sub> and NbS<sub>2</sub> and  
165 suggests that the rate limiting reaction is the desorption of hydrogens. At higher potentials (120 –  
166 250 mV), the Tafel slope increases to ~ 70 mV-dec<sup>-1</sup> (or 65 mV-dec<sup>-1</sup> after *iR* correction),  
167 suggesting that hydrogen adsorption or diffusion of protons to active sites limits the reaction. To  
168 differentiate between these two mechanisms, we made HER measurements under agitation to  
169 increase diffusion of protons and found that the results are largely unchanged. These  
170 observations are consistent with theoretical results that show that, unlike Pt, metallic TMD  
171 catalysts such as NbS<sub>2</sub> possess dilute adsorption of hydrogens on the surface at low potentials but  
172 the high activity per site is retained at higher potentials where coverage of adsorbed hydrogens  
173 increases <sup>4</sup>. In addition to the overpotential and Tafel slope, we have also measured the number  
174 of hydrogen molecules evolved per second (the turnover frequency, TOF) for the catalysts. We  
175 have found that the TOF for the 2H phase Nb<sub>1.35</sub>S<sub>2</sub> catalysts to be in excess of 100 s<sup>-1</sup> at 280 mV.  
176 The TOF from this work compares favorably with other reports, as summarized in Figure 2d.  
177 The exchange current density at 0 V for the Nb<sub>1.35</sub>S<sub>2</sub> phase catalysts was found to be ~ 0.8 mA-  
178 cm<sup>-2</sup> which corresponds to a TOF of 0.17 s<sup>-1</sup>. For comparison, the exchange current density for Pt  
179 (111) is 0.5 – 1 mA-cm<sup>-2</sup> corresponding to TOF of ~ 1 s<sup>-1</sup> (Ref <sup>9</sup>) and for metallic 2D TMDs the  
180 values are 0.02 mA-cm<sup>-2</sup> and 0.043 s<sup>-1</sup> (Ref <sup>3</sup>), suggesting that the turnover for hydrogen  
181 evolution is high for 2H phase Nb<sub>1.35</sub>S<sub>2</sub> catalysts. Summary of the obtained values is provided in  
182 Extended Data Table 1.

183  
184 Impedance measurements on 2H and 3R Nb<sub>1.35</sub>S<sub>2</sub> are shown in Figure 3a. It can be seen that the  
185 series resistance for the 2H phase Nb<sub>1.35</sub>S<sub>2</sub> obtained at 1MHz where the phase angle is close to  
186 zero is 3.5 Ω due to its high electrical conductivity and indicating good contact with glassy  
187 carbon electrode. The charge transfer resistance is 7.4 Ω, facilitating charge injection and  
188 transport to active sites. In contrast, the 3R Nb<sub>1.35</sub>S<sub>2</sub> shows higher resistances and diffusion  
189 limited activity. This is in agreement with our observations that the 3R phase is less conducting  
190 and is stable at higher film thicknesses. Finally, we have measured the electrochemical stability

191 of the electrodes by carrying out over 10000 cycles. The high current density shows remarkable  
192 stability with negligible difference in polarization curves and overpotential values after 10,000  
193 cycles (Figure 3b). The above experimental results suggest that intercalation of Nb between 2H  
194 phase NbS<sub>2</sub> layers to realize Nb<sub>1.35</sub>S<sub>2</sub> allow realization of practical current densities of > 5,000  
195 mA-cm<sup>-2</sup> – making them potentially useful alternatives to Pt and Ir. To translate the high current  
196 densities of 2H phase Nb<sub>1.35</sub>S<sub>2</sub> catalysts into practical device, we fabricated a proof of concept  
197 two electrode electrolyzer for water splitting. The device shown in Figure 3c consists of 2H  
198 Nb<sub>1.35</sub>S<sub>2</sub> on glassy carbon cathode and a commercial Pt anode. The measurements were carried  
199 out at room temperature in 0.5 M H<sub>2</sub>SO<sub>4</sub>. The device characteristics are plotted in Figure 3d,  
200 which show that the reaction for the 2H Nb<sub>1.35</sub>S<sub>2</sub> starts around 1.3 V and the current densities  
201 reach 1000 mA-cm<sup>-2</sup> at 2.0 V. Proof of concept electrolyzers of this type typically report current  
202 densities of 10 – 100 mA-cm<sup>-2</sup> at similar potential values<sup>24</sup>.

203  
204 To elucidate the fundamental mechanisms responsible for the catalytic performance of 2H  
205 Nb<sub>1.35</sub>S<sub>2</sub>, we calculated the thermodynamics of the limiting reaction – the adsorption of hydrogen  
206 on the catalyst surface using density functional theory (DFT) including van der Waals  
207 interactions. It is well known that the best HER catalysts possess  $\Delta G \sim 0$  (that is, thermoneutral  
208 condition) so that there is a driving force for hydrogen adsorption on the active site but the  
209 binding energy is low to allow efficient hydrogen evolution. The results of the calculations are  
210 shown in Figure 4. Our theoretical results suggest that both the Nb and S terminations are stable  
211 for the Nb<sub>1.35</sub>S<sub>2</sub> phases. We have observed intercalated Nb terminated surface by STEM imaging  
212 (see Extended Data Fig. 3d). It can be seen in Figure 4a that the free energy for hydrogen  
213 adsorption for the 2H Nb<sub>1.35</sub>S<sub>2</sub> is close to being thermoneutral ( $\sim 0.11$  eV) when the surface is  
214 terminated by Nb under 0.25 monolayer coverage (Figure 4b). In contrast, the free energy of  
215 adsorbed hydrogen is  $\sim 1$ eV when the surface is terminated by sulfur in 2H Nb<sub>1.35</sub>S<sub>2</sub>. The  
216 calculations also reveal that the reaction is localized to the surface of the catalysts, as indicated  
217 by the charge density diagrams in Figure 4c. The better HER properties of the 2H Nb<sub>1.35</sub>S<sub>2</sub>  
218 relative to the 3R Nb<sub>1.35</sub>S<sub>2</sub> is consistent with the higher density of states at the Fermi level  
219 (Figure 4e,f), which translates into higher measured conductivity and better charge transfer  
220 kinetics. Thus, our work provides new insight into materials design for achieving high current  
221 densities with non-precious metal catalysts.





223 **Figure captions**

224 **Figure 1 | Images of Nb<sub>1+x</sub>S<sub>2</sub> crystals and atomic structure.** **a**, Atomic force microscopy  
225 image of a grown Nb<sub>1+x</sub>S<sub>2</sub> ( $x \sim 0.35$ ) crystals on high quality glassy carbon (scale bar = 1  $\mu\text{m}$ ). **b**,  
226 Cross-sectional ADF STEM image of 2H phase Nb<sub>1.35</sub>S<sub>2</sub> and 3R phase Nb<sub>1+x</sub>S<sub>2</sub>, **c**. The dashed  
227 white rectangle represents the unit cell of the structure and the corresponding ball and stick  
228 model of the unit cell is shown on the right. The red dashed rectangles in the STEM image and  
229 the schematic indicate the positions of the intercalated Nb. Since these sites are partially  
230 occupied, the contrast of these planes is lower than of the fully occupied Nb sites. The arrows  
231 correlate the locations of the atoms in the STEM image with the atoms in the unit cell. The dark  
232 green arrows and spheres in the schematic indicate fully occupied Nb sites and light green  
233 arrows and spheres in unit cell indicate partially occupied Nb atoms. Z. A. refers to zone axis of  
234 the crystal structure. Scale bar = 5  $\text{\AA}$ .

235  
236 **Figure 2 | HER catalytic activities of different TMDs.** **a**, Polarization curves for 2H-MoS<sub>2</sub>,  
237 1T-MoS<sub>2</sub> and WS<sub>2</sub>, 2H-Nb<sub>1.35</sub>S<sub>2</sub>, 3R-Nb<sub>1.35</sub>S<sub>2</sub>, 2H-NbS<sub>2</sub> and 3R NbS<sub>2</sub> and Pt measured in 0.5M  
238 H<sub>2</sub>SO<sub>4</sub> with a scan rate of 5 mVs<sup>-1</sup>. **b**, Expanded view of the low overpotential region in **a**. The  
239 reaction starts immediately upon application of voltage, indicating that the onset potential of 2H-  
240 Nb<sub>1.35</sub>S<sub>2</sub> is < 100 mV and overpotential is 150 mV. **c**, Tafel slopes of different catalysts obtained  
241 from polarization curves in **a**. 2H-Nb<sub>1.35</sub>S<sub>2</sub> shows slope of 43 mV-dec<sup>-1</sup> (38 mV-dec<sup>-1</sup> after *iR*  
242 correction) at low overpotentials (100-130 mV, green) and 70 mV-dec<sup>-1</sup> (65 mV-dec<sup>-1</sup> after *iR*  
243 correction) at high overpotentials (130-200 mV, red). **d**, TOF values of the 2H-Nb<sub>1.35</sub>S<sub>2</sub> (black  
244 line) and other MoS<sub>2</sub>-based catalysts reported in the literature<sup>25,26</sup>. MoS<sub>2</sub> basal planes with sulfur  
245 vacancies (blue)<sup>27</sup>, strained MoS<sub>2</sub> basal planes with sulfur vacancies (green)<sup>27</sup> and MoS<sub>2</sub> with  
246 low charge transfer resistance,  $R_c$  (magenta)<sup>15</sup>.

247  
248 **Figure 3 | Electrochemical impedance spectroscopy (EIS), electrochemical stability of**  
249 **Nb<sub>1.35</sub>S<sub>2</sub> and proof of concept electrolyzer demonstration.** **a**, Nyquist plots of 2H phase (red  
250 curve) and 3R phase Nb<sub>1.35</sub>S<sub>2</sub>. Magnification of 2H-Nb<sub>1.35</sub>S<sub>2</sub> plot is shown in the inset. The plots  
251 (dash line) were fitted using an equivalent circuit to extract the series and charge transfer  
252 resistances. **b**, Polarization curves of 2H-Nb<sub>1.35</sub>S<sub>2</sub> before (black curve) and after (red curve)  
253 10,000 cycles. The insets show the percentage of change in overpotential. The error bars are

254 obtained from at least five measurements. **c**, Photograph of the two electrode electrolyzer device  
255 consisting of commercial Pt anode and 2H-Nb<sub>1.35</sub>S<sub>2</sub> cathode. **d**, Polarization curves of water  
256 electrolysis showing current density of 1000 mA-cm<sup>-2</sup>.

257

258 **Figure 4 | Thermodynamic stability and free-energy calculations for hydrogen evolution for**

259 **2H-Nb<sub>1.35</sub>S<sub>2</sub> and 3R-Nb<sub>1.35</sub>S<sub>2</sub> phases. a**, The free-energy diagram for hydrogen evolution at

260 standard conditions (1 bar of H<sub>2</sub> and pH=0 at 300 K). The energies of the intermediate states are

261 calculated using BEEF-vdW functional as described in the Methods. A coverage of 0.25 ML was

262 used for all calculations. **b**, Optimized geometries for S- and Nb-terminated surfaces of 2H-

263 Nb<sub>1.35</sub>S<sub>2</sub> and 3R-Nb<sub>1.35</sub>S<sub>2</sub> phases. **c**, Charge density difference for H adsorbed on top of Nb-

264 terminated 2H- and 3R-Nb<sub>1.35</sub>S<sub>2</sub> phases. Most of the charge is localized on the surface, with clear

265 differences between 2H- and 3R-Nb<sub>1.35</sub>S<sub>2</sub> phases with the former having larger magnitudes. **e-f**,

266 Density of states (DOS) per atom for Nb-terminated 2H- and 3R-Nb<sub>1.35</sub>S<sub>2</sub> phases projected on

267 different Nb sites. Surface Nb, inner Nb and deep bulk Nb atoms are shown in red, blue and

268 orange, respectively. For a better contrast between the different Nb's atoms, the DOS of surface

269 Nb atoms is highlighted with a filled faint red. Fermi level is set to 0 eV.

270

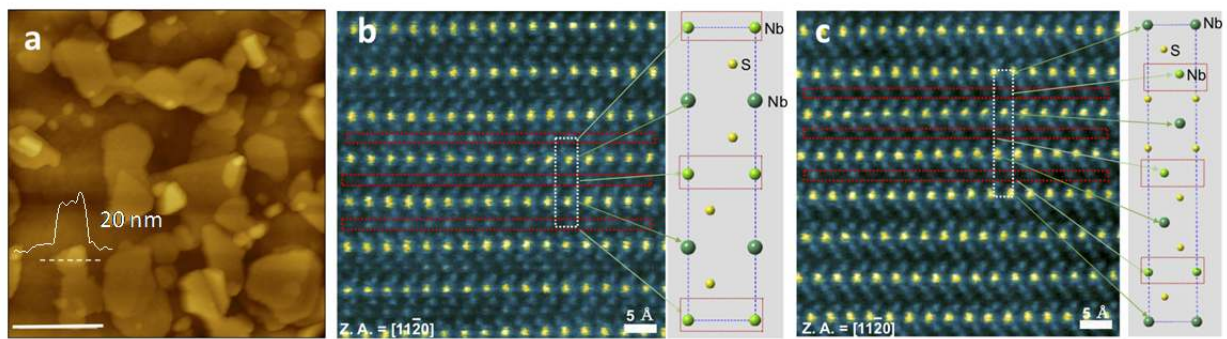
271

272 **Figure 1:**

273

274

275



276

277

278

279

280

281

282

283

284

285

286

287

288

289

290

291

292

293

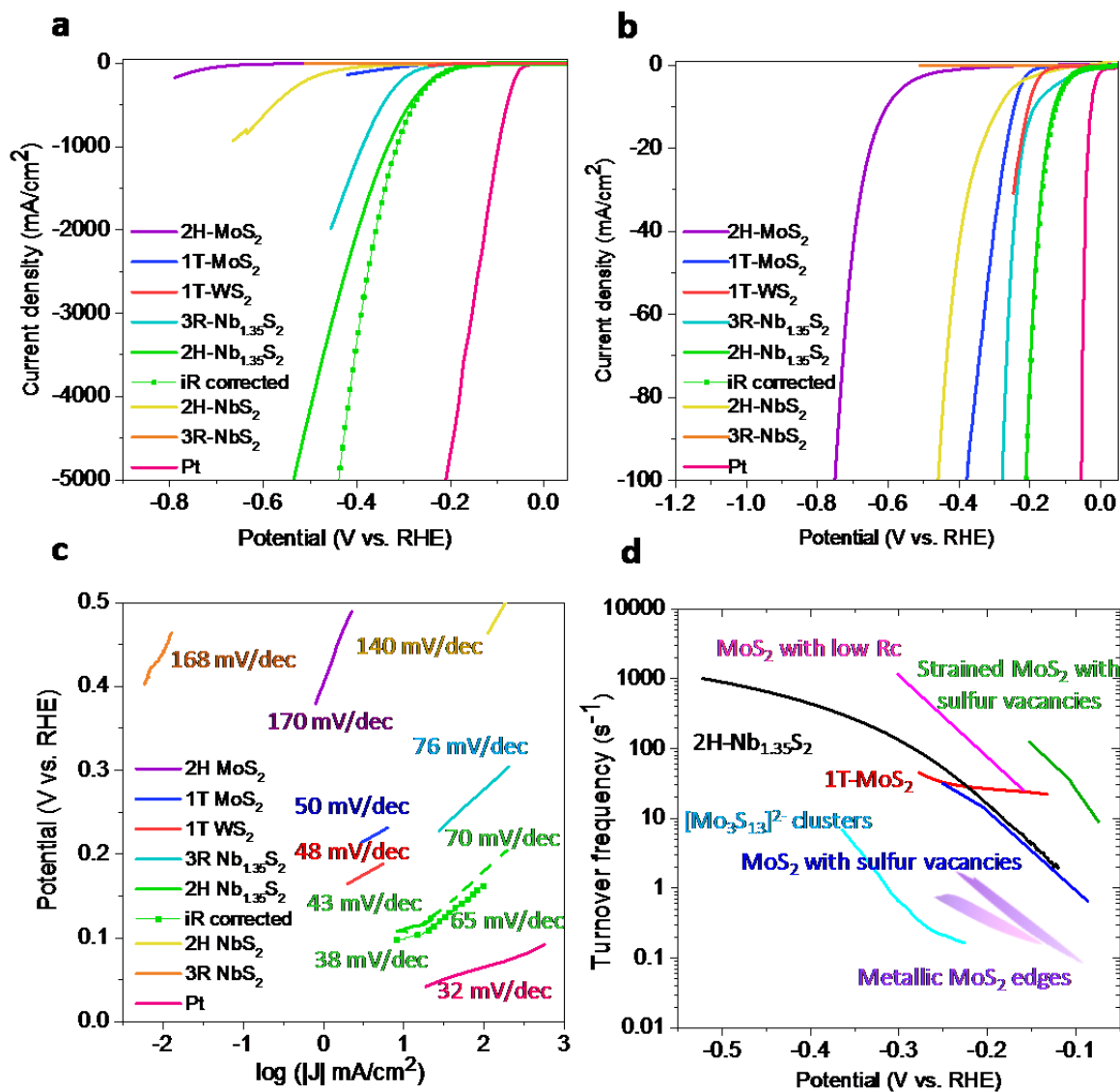
294

295

296

297

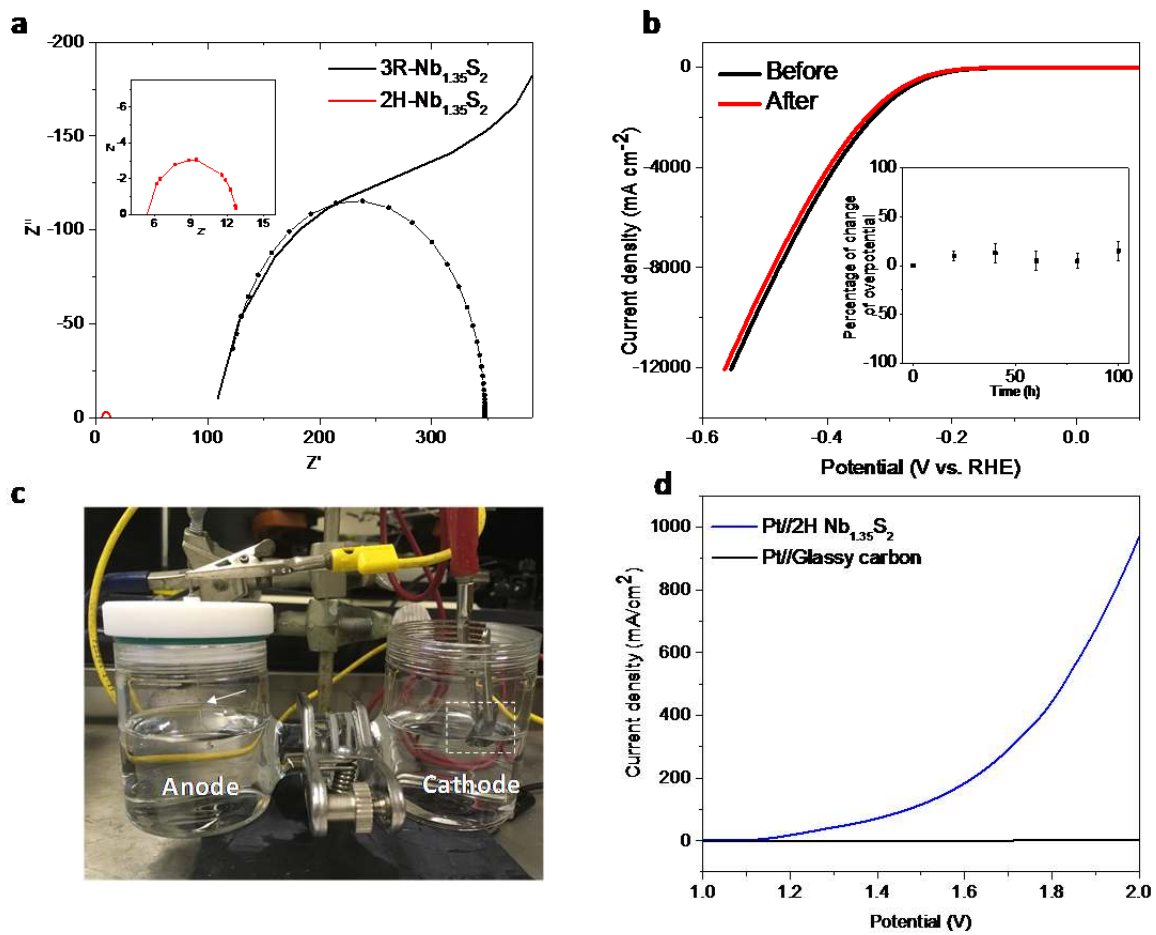
298 **Figure 2**



299

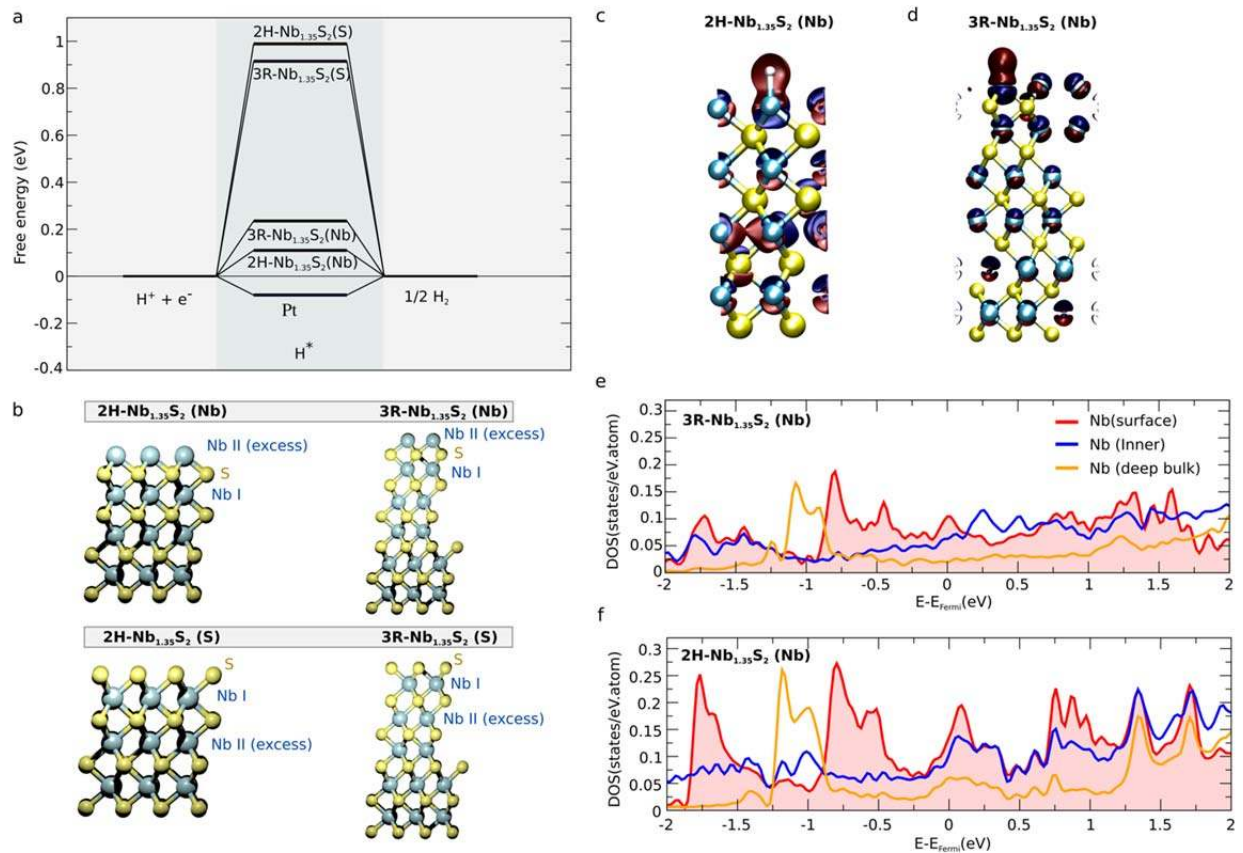
300

301 **Figure 3**  
302  
303



304

305 **Figure 4**  
 306  
 307  
 308  
 309  
 310



311  
 312  
 313  
 314  
 315  
 316  
 317  
 318  
 319  
 320  
 321  
 322  
 323  
 324  
 325  
 326  
 327

328 **References**

329

330 1. Lukowski, M. A. *et al.* Enhanced Hydrogen Evolution Catalysis from Chemically Exfoliated

331 Metallic MoS<sub>2</sub> Nanosheets. *J. Am. Chem. Soc.* **135**, 10274–10277 (2013).

332 2. Voiry, D. *et al.* Conducting MoS<sub>2</sub> Nanosheets as Catalysts for Hydrogen Evolution Reaction.

333 *Nano Lett.* **13**, 6222–6227 (2013).

334 3. Voiry, D. *et al.* Enhanced catalytic activity in strained chemically exfoliated WS<sub>2</sub> nanosheets

335 for hydrogen evolution. *Nat. Mater.* **12**, 850 (2013).

336 4. Liu, Y. *et al.* Self-optimizing, highly surface-active layered metal dichalcogenide catalysts for

337 hydrogen evolution. *Nat. Energy* **2**, 17127 (2017).

338 5. Shi, J. *et al.* Two-dimensional metallic tantalum disulfide as a hydrogen evolution catalyst.

339 *Nat. Commun.* **8**, 958 (2017).

340 6. Li, H. *et al.* Atomic-Sized Pores Enhanced Electrocatalysis of TaS<sub>2</sub> Nanosheets for Hydrogen

341 Evolution. *Adv. Mater.* **28**, 8945–8949 (2016).

342 7. Yuan, J. *et al.* Facile Synthesis of Single Crystal Vanadium Disulfide Nanosheets by

343 Chemical Vapor Deposition for Efficient Hydrogen Evolution Reaction. *Adv. Mater.* **27**,

344 5605–5609 (2015).

345 8. Chia, X., Ambrosi, A., Lazar, P., Sofer, Z. & Pumera, M. Electrocatalysis of layered Group 5

346 metallic transition metal dichalcogenides (MX<sub>2</sub>, M = V, Nb, and Ta; X = S, Se, and Te). *J.*

347 *Mater. Chem. A* **4**, 14241–14253 (2016).

348 9. Jaramillo, T. F. *et al.* Identification of Active Edge Sites for Electrochemical H<sub>2</sub> Evolution

349 from MoS<sub>2</sub> Nanocatalysts. *Science* **317**, 100–102 (2007).



- 350 10. Zhiqiang, S., Baolian, Y. & Ming, H. Bifunctional electrodes with a thin catalyst layer for  
351 'unitized' proton exchange membrane regenerative fuel cell. *J. Power Sources* **79**, 82–85  
352 (1999).
- 353 11. Altmann, S., Kaz, T. & Friedrich, K. A. Bifunctional electrodes for unitised regenerative  
354 fuel cells. *Electrochimica Acta* **56**, 4287–4293 (2011).
- 355 12. Jellinek, F., Brauer, G. & Müller, H. Molybdenum and Niobium Sulphides. *Nature* **185**,  
356 376 (1960).
- 357 13. Merki, D. & Hu, X. Recent developments of molybdenum and tungsten sulfides as  
358 hydrogen evolution catalysts. *Energy Environ. Sci.* **4**, 3878–3888 (2011).
- 359 14. Benck, J. D., Hellstern, T. R., Kibsgaard, J., Chakthranont, P. & Jaramillo, T. F.  
360 Catalyzing the Hydrogen Evolution Reaction (HER) with Molybdenum Sulfide  
361 Nanomaterials. *ACS Catal.* **4**, 3957–3971 (2014).
- 362 15. Voiry, D. *et al.* The role of electronic coupling between substrate and 2D MoS<sub>2</sub>  
363 nanosheets in electrocatalytic production of hydrogen. *Nat. Mater.* **15**, 1003 (2016).
- 364 16. Yin, Y. *et al.* Contributions of Phase, Sulfur Vacancies, and Edges to the Hydrogen  
365 Evolution Reaction Catalytic Activity of Porous Molybdenum Disulfide Nanosheets. *J. Am.*  
366 *Chem. Soc.* **138**, 7965–7972 (2016).
- 367 17. Kibsgaard, J., Chen, Z., Reinecke, B. N. & Jaramillo, T. F. Engineering the surface  
368 structure of MoS<sub>2</sub> to preferentially expose active edge sites for electrocatalysis. *Nat. Mater.*  
369 **11**, 963 (2012).
- 370 18. Kong, D. *et al.* Synthesis of MoS<sub>2</sub> and MoSe<sub>2</sub> Films with Vertically Aligned Layers.  
371 *Nano Lett.* **13**, 1341–1347 (2013).

- 372 19. Tsai, C., Abild-Pedersen, F. & Nørskov, J. K. Tuning the MoS<sub>2</sub> Edge-Site Activity for  
373 Hydrogen Evolution via Support Interactions. *Nano Lett.* **14**, 1381–1387 (2014).
- 374 20. Eda, G. *et al.* Photoluminescence from Chemically Exfoliated MoS<sub>2</sub>. *Nano Lett.* **11**,  
375 5111–5116 (2011).
- 376 21. Pan, H. Metal Dichalcogenides Monolayers: Novel Catalysts for Electrochemical  
377 Hydrogen Production. *Sci. Rep.* **4**, 5348 (2014).
- 378 22. Tsai, C., Chan, K., Nørskov, J. K. & Abild-Pedersen, F. Theoretical insights into the  
379 hydrogen evolution activity of layered transition metal dichalcogenides. *Surf. Sci.* **640**, 133–  
380 140 (2015).
- 381 23. Yu, Y. *et al.* Layer-Dependent Electrocatalysis of MoS<sub>2</sub> for Hydrogen Evolution. *Nano*  
382 *Lett.* **14**, 553–558 (2014).
- 383 24. Han, N. *et al.* Nitrogen-doped tungsten carbide nanoarray as an efficient bifunctional  
384 electrocatalyst for water splitting in acid. *Nat. Commun.* **9**, 924 (2018).
- 385 25. Kibsgaard, J., Jaramillo, T. F. & Besenbacher, F. Building an appropriate active-site  
386 motif into a hydrogen-evolution catalyst with thiomolybdate [Mo<sub>3</sub>S<sub>13</sub>]<sup>2-</sup> clusters. *Nat. Chem.*  
387 **6**, 248 (2014).
- 388 26. Xie, J. *et al.* Defect-Rich MoS<sub>2</sub> Ultrathin Nanosheets with Additional Active Edge Sites  
389 for Enhanced Electrocatalytic Hydrogen Evolution. *Adv. Mater.* **25**, 5807–5813 (2013).
- 390 27. Li, H. *et al.* Activating and optimizing MoS<sub>2</sub> basal planes for hydrogen evolution through  
391 the formation of strained sulphur vacancies. *Nat. Mater.* **15**, 48 (2016).

392  
393  
394  
395  
396

397 **Acknowledgments:** MC, JY acknowledge financial support from AFOSR FA9550-16-1-0289.  
398 MC, YW acknowledge support from NSF ECCS-1608389. MC and XS acknowledge support  
399 from Shenzhen Peacock Plan (Grant No. KQTD2016053112042971). MC and ARM  
400 acknowledge financial support from the Ministry of Higher Education Malaysia. HYJ  
401 acknowledges the support from Creative Materials Discovery Program through the National  
402 Research Foundation of Korea (NRF-2016M3D1A1900035). E.J.G.S. acknowledges the use of  
403 computational resources from the UK national high-performance computing service (ARCHER)  
404 for which access was obtained via the UKCP consortium (EPSRC grant ref EP/K013564/1); the  
405 UK Materials and Molecular Modelling Hub for access to THOMAS supercluster, which is  
406 partially funded by EPSRC (EP/P020194/1). The Queen's Fellow Award through the grant  
407 number M8407MPH, the Enabling Fund (A5047TSL), and the Department for the Economy  
408 (USI 097) are also acknowledged.

409

#### 410 **Author Contributions**

411 MC conceived the idea and supervised the project. JY and ARM designed the experiments with  
412 guidance from MC. JY performed the electrochemical measurements and analyses with advice  
413 from RF and DV. ARM synthesized the  $\text{Nb}_{1.35}\text{S}_2$  samples and characterized them. YW made the  
414 devices for HER measurements and made electrical measurements. XS and IB made  $\text{NbS}_2$   
415 samples and characterized them with the help of FZ. HYJ prepared the FIB samples, performed  
416 the STEM analyses on the samples. MA and EJGS provided theoretical insight for the  
417 experimental results. MC, HYJ, JY, DV, RF and HS analyzed the data. MC wrote the paper with  
418 JY and all of the authors edited the manuscript before submission.

419

420

421

422

423

424

425

426

427

428

429

430

431 **Methods**

432 **Growth of 2H-Nb<sub>1+x</sub>S<sub>2</sub> and 3R-Nb<sub>1+x</sub>S<sub>2</sub>:** Nb<sub>1+x</sub>S<sub>2</sub> growth was achieved under low pressure in a  
433 horizontal furnace (Lindberg/Blue M) with 1-inch diameter quartz tube. Two small quartz tubes  
434 (diameter ~ 9mm) loaded with niobium chloride (NbCl<sub>5</sub>, Alfa Aesar, 99.9%) and sulfur powder  
435 (Alfa Aesar, 99.5%), were placed upstream of the furnace as shown in Extended Data Fig. 6. The  
436 substrates (SiO<sub>2</sub>/Si and glassy carbon) were placed face up above an alumina boat in the center  
437 zone of the furnace. The tube was initially pumped to a base pressure of 20 Torr for 30min. The  
438 furnace was heated up to 850 °C with a ramp rate of 55 °C/min with a flow of 90 sccm Ar. Then,  
439 the furnace was heated up to 1000 °C with a ramp rate of 6 °C/min under a flow of 90 sccm  
440 H<sub>2</sub>/Ar (10% H<sub>2</sub> in Ar). The NbCl<sub>5</sub> was sublimated via a heating belt at 260~300 °C within 5min  
441 when the furnace reached to 1000 °C as indicated by the heating cycle shown in Extended Data  
442 Fig. 7. After growth for 8 min at 1000 °C, the whole system was naturally cooled down to room  
443 temperature.

444  
445 **Synthesis of 2H-NbS<sub>2</sub>:** 2H-NbS<sub>2</sub> was synthesized by CVD using niobium oxide (Nb<sub>2</sub>O<sub>5</sub>, 99.9%  
446 Sigma-Aldrich) mixed with alkali halide (potassium iodine, KI) and sulfur powder (99.5%, Alfa  
447 Aesar). Since niobium oxide has a high melting point, alkali halide is used to create a new  
448 eutectic point for the reaction to produce more volatile oxides.<sup>28</sup> The mixture of 150 mg of  
449 Nb<sub>2</sub>O<sub>5</sub> and 100 mg of KI powders in alumina boat was loaded at the center of the tube furnace  
450 and SiO<sub>2</sub> substrates were placed above the powder with its polished side facing down. 100 mg of  
451 S powder was loaded in the upstream region of the tube. Then, 80 sccm carrier gas (10 % of H<sub>2</sub>  
452 in Ar) was introduced for 20 min to remove oxygen in the furnace. The furnace was heated with  
453 a ramp rate of 33 °C/min to the growth temperatures (1000 °C) and held at 1000 °C for 30 min  
454 before cooling down. The upstream region reached 200 °C during the growth. The thin 2H NbS<sub>2</sub>  
455 crystals and their corresponding Raman spectrum are shown in Extended Data Fig. 8a,b.

456  
457 **Synthesis of 3R-NbS<sub>2</sub>:** 3R-NbS<sub>2</sub> crystals were grown by a chemical vapor transport (CVT)  
458 method which has been employed to prepare other layered compounds.<sup>29</sup> Prior to crystal growth,  
459 a quartz tube containing high purity source (Nb 99.99% and S 99.99% with a molar ratio of Nb:S  
460 is 1:2) was evacuated at 10<sup>-6</sup> Torr and sealed. The sealed quartz tube was then inserted into the  
461 tube furnace. The furnace was heated up to 900 °C with a ramp rate of 3°C/min. The reaction

462 time was 18 h at 900 °C and the furnace was cooled down naturally. The CVT grown 3R crystals  
463 and the corresponding Raman spectrum are shown in Extended Data Fig. 8c,d.

464  
465 **Electrochemical measurements:** Electrochemical measurements were performed in a three-  
466 electrode cell using a Versa Stat 3 potentiostat from Princeton Applied research. All  
467 measurements were made in 0.5 M H<sub>2</sub>SO<sub>4</sub> electrolyte purged with Ar gas. A saturated calomel  
468 electrode (Pine Instrument) and glassy carbon were used as the reference electrode and counter  
469 electrode, respectively. Extended Data Fig. 9 shows the polarization curves obtained from 2H  
470 Nb<sub>1.35</sub>S<sub>2</sub> using platinum and carbon counter electrode. No noticeable difference was observed,  
471 and this excludes any Pt contamination during the measurements. The glassy carbon plate (Ted  
472 pella) loaded with 3R- and 2H-Nb<sub>1.35</sub>S<sub>2</sub> was used as a working electrode. 3R-NbS<sub>2</sub> was dispersed  
473 into toluene and sonicated for 1h. The solution was deposited onto glassy carbon electrode (0.1  
474 mg/cm<sup>2</sup>) and dried. 1T-MoS<sub>2</sub> was prepared by the exfoliation of 2H-MoS<sub>2</sub> by n-BuLi following  
475 literature.<sup>20</sup> 1T-MoS<sub>2</sub> solution was loaded onto glassy carbon electrode (4 μg/cm<sup>2</sup>) and 2H-MoS<sub>2</sub>  
476 powder is dispersed into the mixed solution with DI water/IPA (the volume ratio 4:1) and  
477 sonicated for 1h to drop onto the glassy carbon electrode. All polarization curves were measured  
478 at the scan rate of 5 mVs<sup>-1</sup>. All potentials are referenced to RHE. In 0.5 M H<sub>2</sub>SO<sub>4</sub>,  
479 E(RHE)=E(SCE) + 0.254 V. Impedance measurements were performed at -0.22 V versus RHE  
480 from 1MHz to 0.1 Hz with a 5 mV a.c. amplitude.

481  
482 **Device fabrication of 2H-NbS<sub>2</sub>:** To demonstrate the HER performance of 2H-NbS<sub>2</sub>, we carried  
483 out HER test using an electrochemical microcell.<sup>15</sup> We performed e-beam lithography to put gold  
484 contacts on as-grown 2H-NbS<sub>2</sub> on SiO<sub>2</sub> (300 nm) substrate. The gold electrodes were deposited  
485 via e-beam evaporation under high vacuum conditions (10<sup>-7</sup> Torr). After this process, we  
486 performed another e-beam lithography step to open a window on 2H-NbS<sub>2</sub> and cover the gold  
487 electrodes to avoid contact with electrolyte. The device is shown in Extended Data Fig. 10.  
488 Electrochemical measurements were performed in 0.5 M H<sub>2</sub>SO<sub>4</sub> and glassy carbon and Ag/AgCl  
489 electrodes were used as counter and reference electrodes, respectively.

490  
491

492 **Electrochemical surface area measurements:** The estimation of electrochemically active  
 493 surface area was conducted by measurement of the double-layer capacitance in a potential region  
 494 with no faradaic response. Cyclic voltammetric (CV) measurements were performed between  
 495 285 mV and 315 mV vs. RHE at various scan rates from 5 mVs<sup>-1</sup> to 100 mVs<sup>-1</sup> in order to  
 496 estimate the double layer capacitance (C<sub>dl</sub>), see Extended Data Fig. 5. Roughness factor (RF) was  
 497 estimated from the ratio of the measured double layer capacitance with respect to the specific  
 498 capacitance of glassy carbon electrode (0.87 mF/cm<sup>2</sup>). Our image analysis of the electrode  
 499 surface (Extended Data Fig. 4) shows that only ~ 20% of the glassy carbon electrode is covered  
 500 by the catalyst. Therefore, to calculate the RF, we take the areal capacitance of the glassy carbon  
 501 after catalyst deposition to be (0.87 mF-cm<sup>-2</sup>)(0.8) = 0.7 mF-cm<sup>-2</sup>. Thus, the RF is given by:

$$RF = \frac{9.6 \text{ mF cm}^{-2}}{0.7 \text{ mF cm}^{-2}} = 13.7$$

504 **Turnover frequency calculation:** According to previous literature, turnover frequency can be  
 505 obtained following equation.

$$TOF (s^{-1}) = \frac{J \left( \frac{A}{cm^2} \right)}{n \times N \times RF \times (1.602 \times 10^{-19} C)}$$

506 To determine the density of active sites (*N*), we assume the lattice constant of 2H-Nb<sub>1.35</sub>S<sub>2</sub> is 3.31  
 507 Å (Figure 1c, STEM image). *n* is the number of electrons involved in the reaction. The surface  
 508 area of unit cell can be 9.4 x 10<sup>-16</sup> cm<sup>2</sup>. We assumed that entire basal plane can be catalytically  
 509 active. Therefore, the density of active is estimated to be about 1.06 x 10<sup>15</sup> cm<sup>-2</sup>. The density of  
 510 the surface active sites of 2H Nb<sub>1.35</sub>S<sub>2</sub> on geometric area : 1.06 x 10<sup>15</sup> sites/cm<sup>2</sup> x 13.7 = 1.4 x  
 511 10<sup>16</sup> sites/cm<sup>2</sup>

512 To get TOF at exchange current density, the exchange current density was extrapolated linearly  
 513 from the Tafel slope. The exchange current density of 2H-Nb<sub>1.35</sub>S<sub>2</sub> is 800 μA/cm<sup>2</sup> which is  
 514 remarkable value among the reported TMD based catalysts as listed in Extended Data Table 1.

515  
 516 **Electrical conductivity measurements:** The conductivity of the intercalated phases was  
 517 measured and by evaporating gold contacts and is shown in Extended Data Fig. 11. We find the  
 518 2H Nb<sub>1.35</sub>S<sub>2</sub> phase to be highly conducting compared to other reports in the literature.<sup>30-33</sup>

519

520 **Computational Methods:** The calculations were done using the plane wave density functional  
521 theory (DFT) Vienna ab-initio simulation package (VASP)<sup>34-37</sup> The van der Waals interactions  
522 were taken into account at the level of opt-B88 functional<sup>38</sup> and the Bayesian error estimation  
523 exchange-correlation functional with long-range interactions<sup>39</sup> (BEEF-vdW). A 500 eV plane-  
524 wave cutoff was used, and the Brillouin zone was sampled with a Monkhorst-Pack<sup>40</sup> sampling of  
525 3x3x1 k-points grid for the relaxation and a 15x15x1 k-points for the energy calculations. The  
526  $\Delta G_H$  were calculated using the formula:

$$\Delta G_H = \Delta E + \Delta(ZPE) - T\Delta S$$

528  
529 with  
530

$$\Delta E = E(\text{surface} + H) - E(\text{surface}) - \frac{1}{2}E(H_2)$$

531

$$\Delta(ZPE) = ZPE_H - \frac{1}{2}ZPE_{H_2}$$

532

$$T\Delta S = \frac{-1}{2}TS_{H_2} = -0.205eV$$

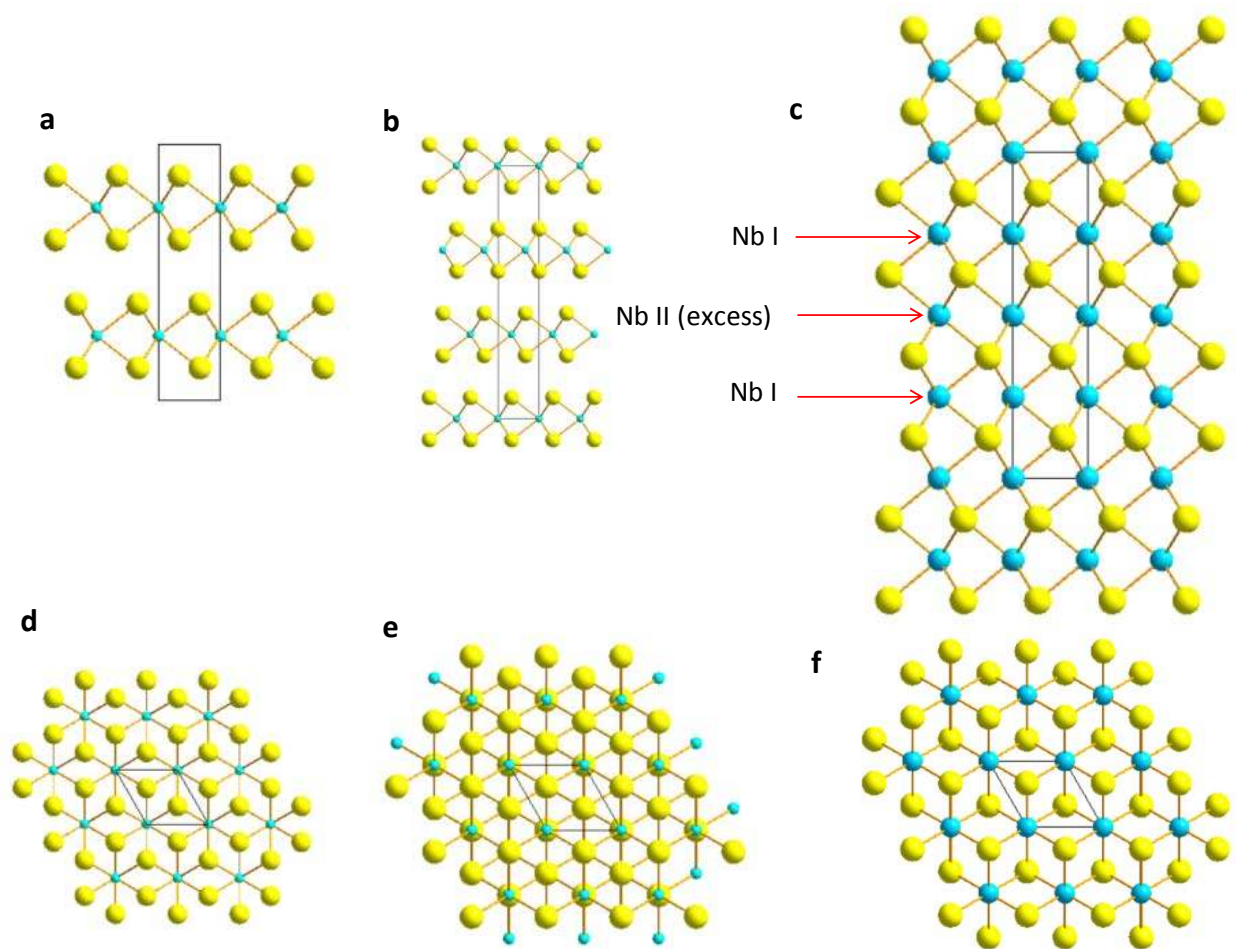
533

534

535 Where  $E(\text{surface} + H)$  is the total energy of the system with the H-atom bound at the basal  
536 plane,  $E(\text{surface})$  is the total energy of the pristine system,  $E(H_2)$  is the total energy of the  $H_2$   
537 molecule.  $\Delta(ZPE)$  is the difference between the zero-point energy (ZPE) of the H-atom and the  
538 zero-point energy of the  $H_2$  molecule, calculated using the normal mode analysis. We will use  
539 the entropy of the molecular hydrogen in the gas phase at standard conditions (1 bar of  $H_2$ , pH=0  
540 and T=300 K).

541 The bulk lattice parameters calculated using ab initio opt B88-vdW and BEEF-vdW functionals  
542 are shown in Extended Data Tables 3 and 5, as well their energetics as displayed in Extended  
543 Tables 4, 6, 7 and 8. The corresponding crystal structures obtained from these parameters are  
544 shown in Extended Data Figure 12.

545  
546  
547  
548

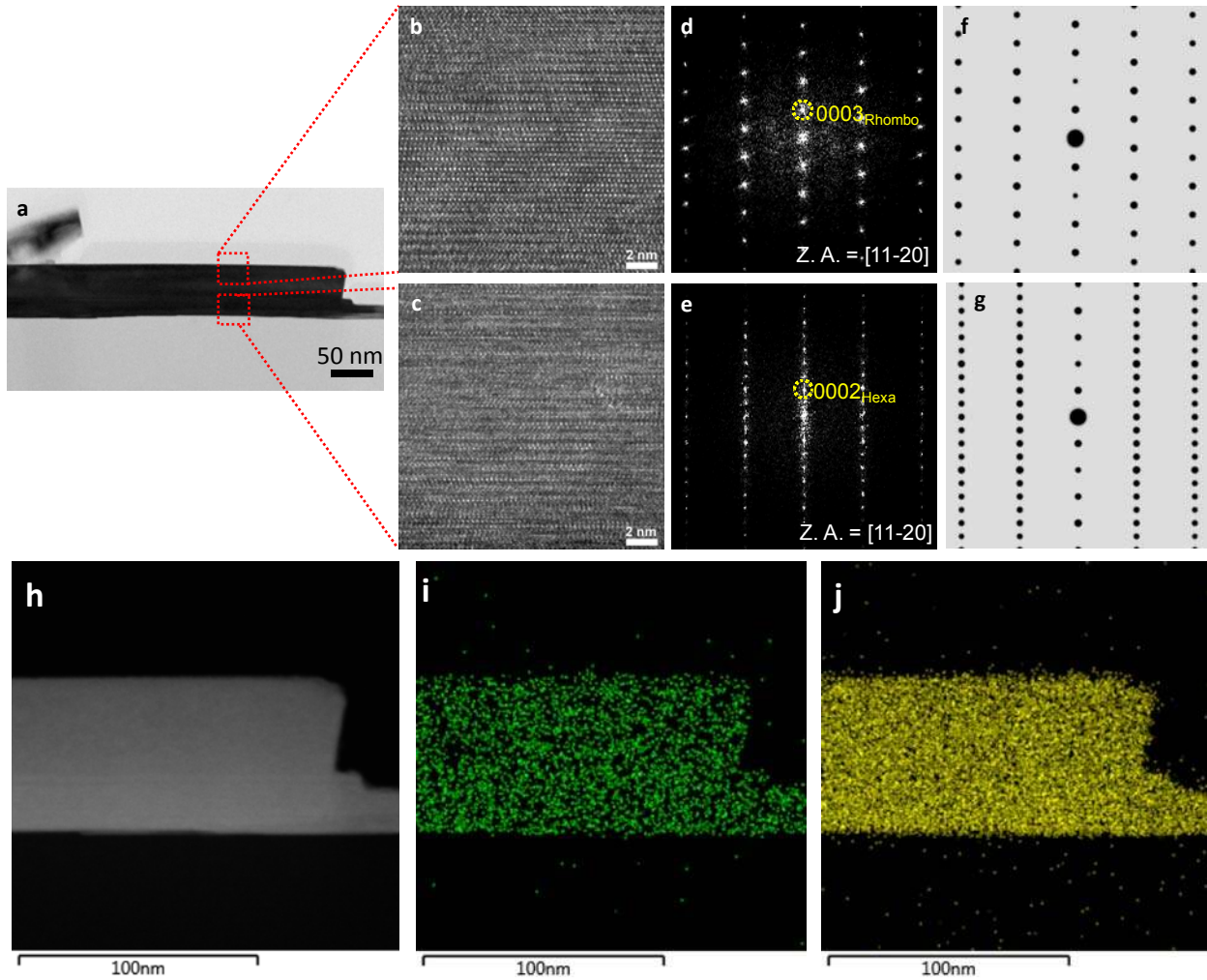


549  
550 **Extended Data Fig. 1 | Phases of NbS<sub>2</sub>.** (a, b) Side view and (d, e) top view of 2H hexagonal  
551 (P63/mmc symmetry) and 3R rhombohedral (R3m symmetry) phases of NbS<sub>2</sub>. (c, f) Side and top  
552 views of 2H phase Nb<sub>1.35</sub>S<sub>2</sub> phase. The excess of Nb (labelled as Nb II in the c) occupies  
553 octahedral configuration while the Nb I are in trigonal prismatic sites. The Nb<sub>1.35</sub>S<sub>2</sub> phase can  
554 also occur in the 3R phase.

555  
556  
557  
558



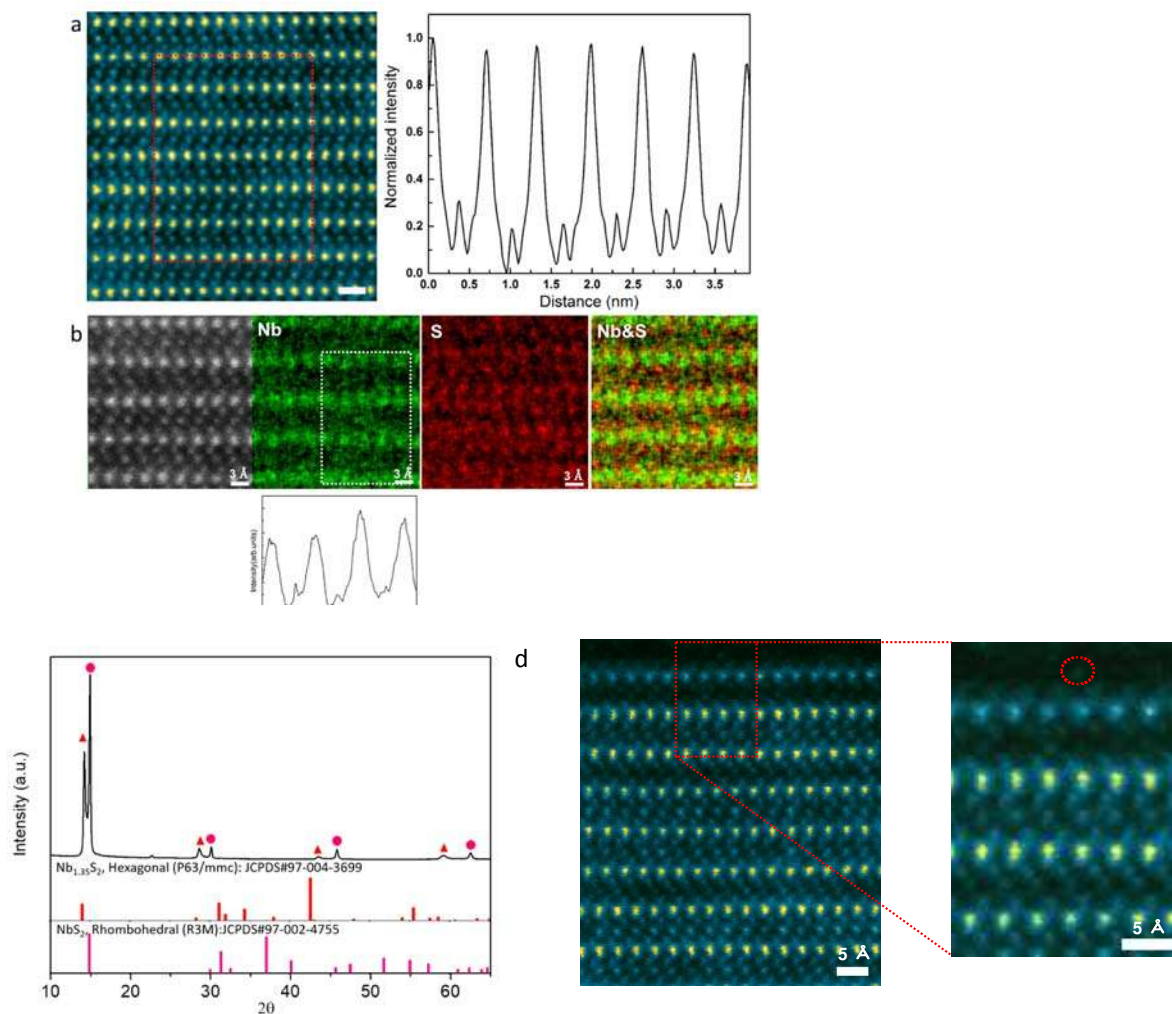
559  
560



561

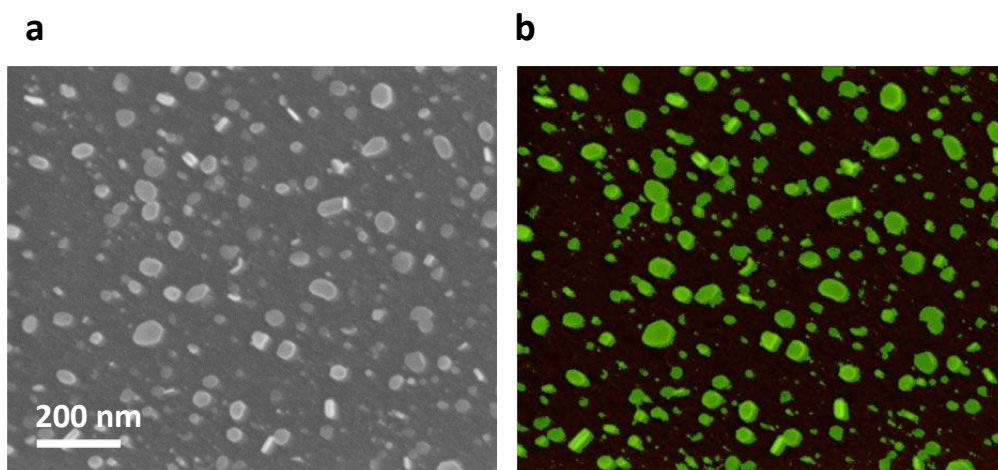
562

563 **Extended Data Fig. 2 | TEM of Nb<sub>1.35</sub>S<sub>2</sub> and corresponding diffraction images.** **a**, Low  
564 magnification BFTEM image of cross-sectional FIB sample (thickness = 40 nm) prepared from  
565 CVD grown samples on SiO<sub>2</sub>. **b**, **c** HRTEM images taken from top of the sample and bottom of  
566 the sample as indicated by square dotted regions on the left image. **d**, **e** Fast Fourier transform  
567 (FFT) pattern indicating that the top (thicker) region is rhombohedral while the bottom (thin)  
568 region is in hexagonal configuration based on their very good agreement with simulated patterns  
569 shown in **f** (simulated ED patterns for intercalated 3R phase) and **g** (simulated ED for  
570 intercalated 2H phase). **h**, Low magnification of image of the FIB cross section and the  
571 corresponding Energy Dispersive Spectroscopy map showing Nb (**i**) and S (**j**) in the sample.

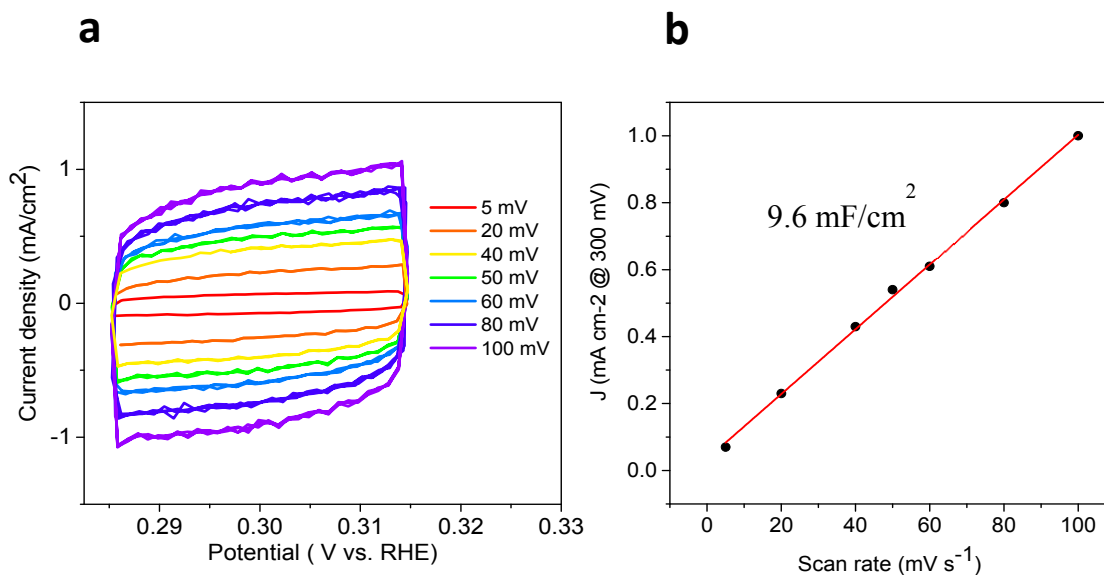


572  
 573 **Extended Data Fig. 3 | Line scan and chemical analyses in STEM.** **a,** Annular dark field  
 574 image (left) and the corresponding (right) intensity line scan of  $2H\text{-Nb}_{1.35}\text{S}_2$  phase showing that  
 575 Nb atoms are present between the layers. **Scale bar = 5 Å.** **b,** Black and white unfiltered STEM  
 576 image and corresponding elemental maps of Nb, S, and both Nb and S obtained using energy  
 577 dispersive x-ray spectroscopy. The mapping and the line scan below the Nb map confirm that the  
 578 intercalated atoms are Nb. **c,** X-ray diffraction of  $\text{Nb}_{1.35}\text{S}_2$ . The spectrum matches JCPDS#97-  
 579 004-3699 for hexagonal phase  $\text{Nb}_{1.35}\text{S}_2$ , indicated by the triangles. In particular, the presence of  
 580 additional diffraction peak at  $\sim 14.3^\circ$  indicates excess Nb. The structure is a combination of  
 581 layered  $\text{NbS}_2$  and intercalated  $2H\text{-Nb}_{1.35}\text{S}_2$  – completely consistent with our STEM results. **d,**  
 582 STEM image of  $2H$  phase  $\text{Nb}_{1.35}\text{S}_2$  with an enlargement of the surface region shown on the right.  
 583 Faint images of Nb atoms terminating the surface can be observed as indicated by the dotted red  
 584 circle.

585  
586  
587  
588  
589  
590  
591  
592  
593  
594  
595  
596  
597  
598  
599

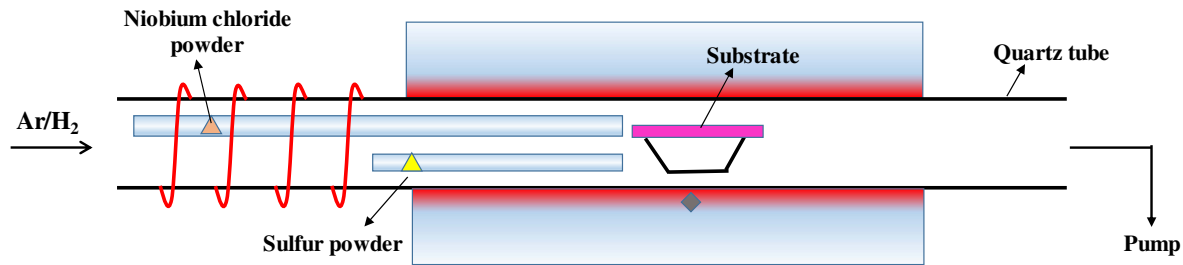


600 **Extended Data Fig. 4 | Image analyses of areal coverage of catalysts on electrode surface. a,**  
601 **SEM image of 2H-Nb<sub>1.35</sub>S<sub>2</sub>. b, Image analyses was used to highlight (in green) the Nb<sub>1.35</sub>S<sub>2</sub>**  
602 **flakes on the glassy carbon electrode (black background). Then the percent of area covered by**  
603 **the flakes was calculated. A total of 15 images were taken and the average area covered by the**  
604 **catalyst Nb<sub>1.35</sub>S<sub>2</sub> flakes was approximately 20 % ± 3% of the electrode surface.**



605

606 **Extended Data Fig. 5 | Electrochemical surface area measurements. a,** CV curves of Nb<sub>1.35</sub>S<sub>2</sub>  
607 electrodes measured between 285 and 315 mV vs. RHE. **b,** Current density at 300 mV plotted  
608 against cyclic voltammetry scan rate.  
609  
610



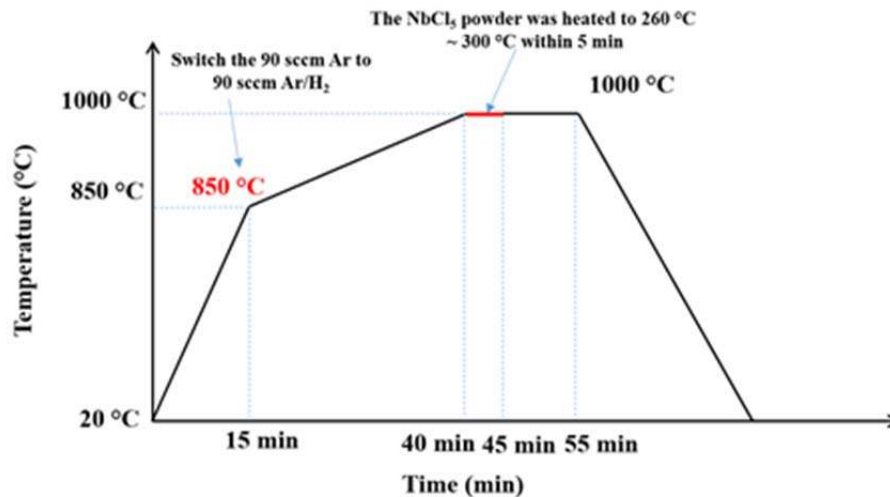
611

612 **Extended Data Fig. 6 | Schematic of chemical vapor deposition setup for Nb<sub>1+x</sub>S<sub>2</sub> synthesis.**

613 The precursors are placed upstream because they sublime at a much lower temperature than the  
614 growth temperature.

615

616



617

618 **Extended Data Fig. 7 | Heating ramp and cooling cycle growth of Nb<sub>1+x</sub>S<sub>2</sub>.** The tube furnace

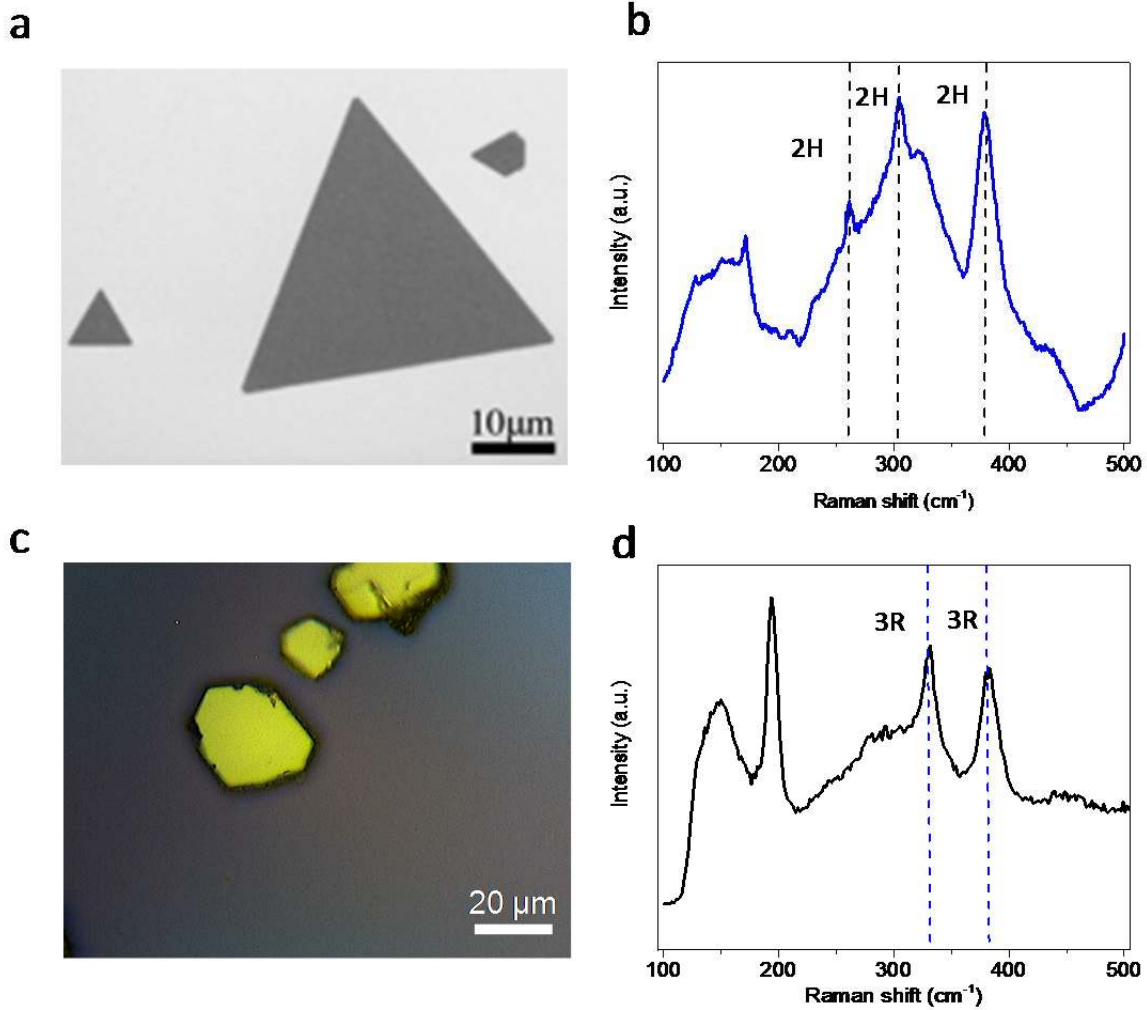
619 was initially heated in Ar atmosphere, then in reducing atmosphere and growth was conducted  
620 for 10 – 20 minutes to achieve different thicknesses.

621

622

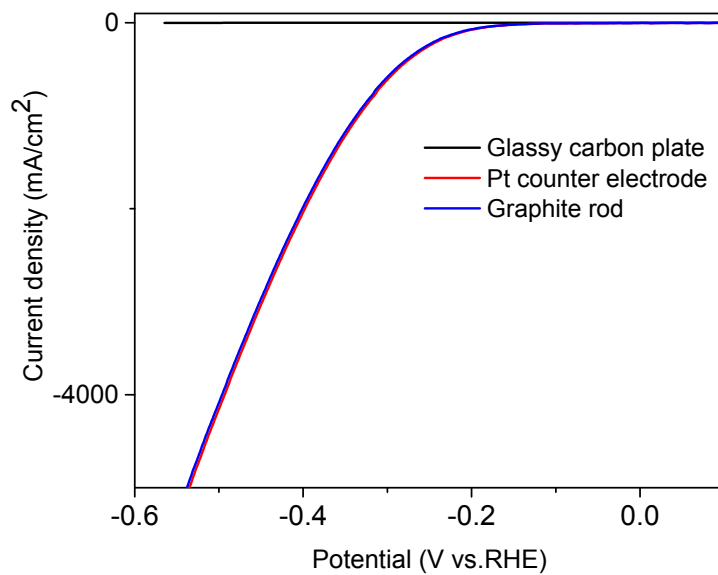
623

624



625  
 626 **Extended Data Fig. 8 | Different phases of NbS<sub>2</sub>.** **a**, SEM image of CVD grown 2H-NbS<sub>2</sub> with  
 627 lateral dimensions of 5-20 μm and **b**, Raman spectrum of 2H-NbS<sub>2</sub> shows E<sub>1g</sub>, E<sup>1</sup><sub>1g</sub>, A<sub>1g</sub> at 260,  
 628 304 and 379 cm<sup>-1</sup> respectively. **c**, Optical microscope image of 3R-NbS<sub>2</sub> grown by CVT and **d**,  
 629 Raman spectrum of 3R-NbS<sub>2</sub> shows E<sub>2g</sub> and A<sub>1g</sub> peaks at 330 cm<sup>-1</sup> and 385 cm<sup>-1</sup>, respectively.

630  
 631  
 632  
 633  
 634  
 635  
 636



637

638 **Extended data Fig. 9** | Pt vs glassy carbon as counter electrode. Polarization curves for glassy  
639 carbon plate and 2H Nb<sub>1.35</sub>S<sub>2</sub> using Pt or carbon as counter electrode.

640

641

642

643

644

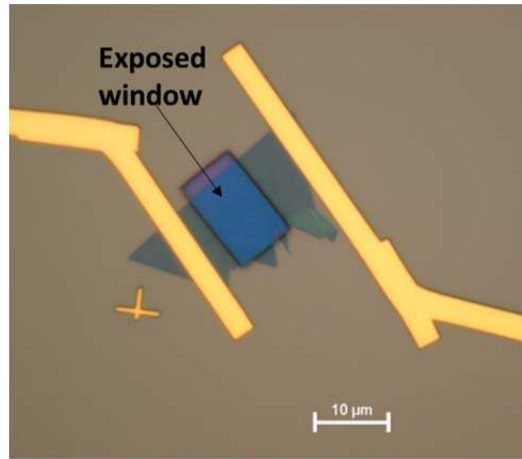
645

646

647

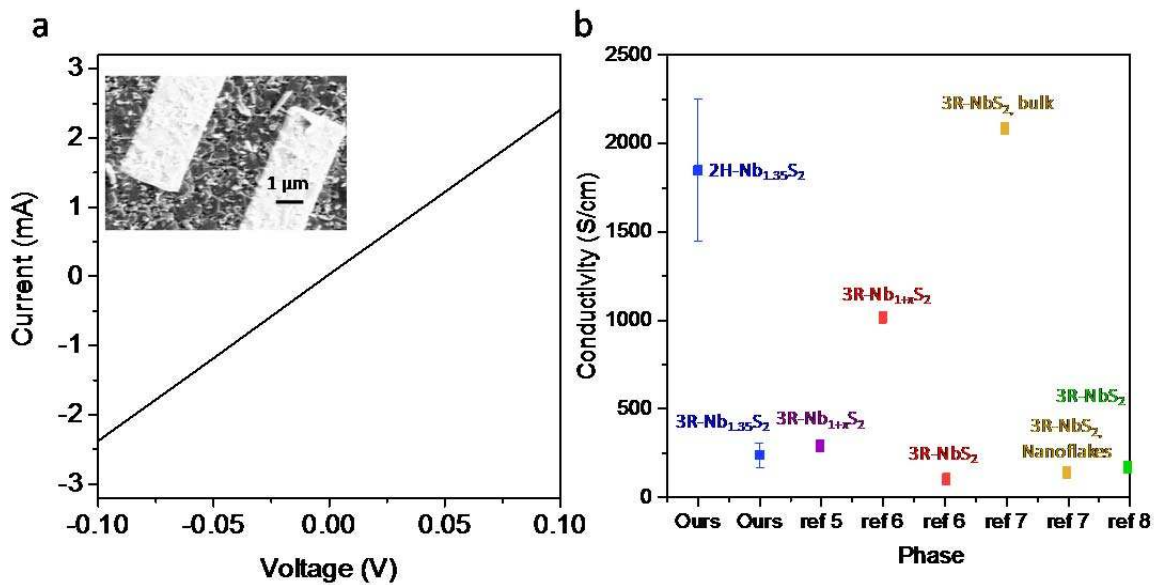
648





649  
650

651 **Extended data Fig. 10 | Electrochemical microcell devices.** Optical image of an  
652 electrochemical microcell with 2H-NbS<sub>2</sub> as the catalyst. The blue region is the NbS<sub>2</sub> flake and  
653 rectangular gold contacts are patterned onto it. A window is opened lithographically so that  
654 catalysis measurements can be made. The entire area is covered by PMMA except the window so  
655 the electrolyte can only interact with the catalyst.



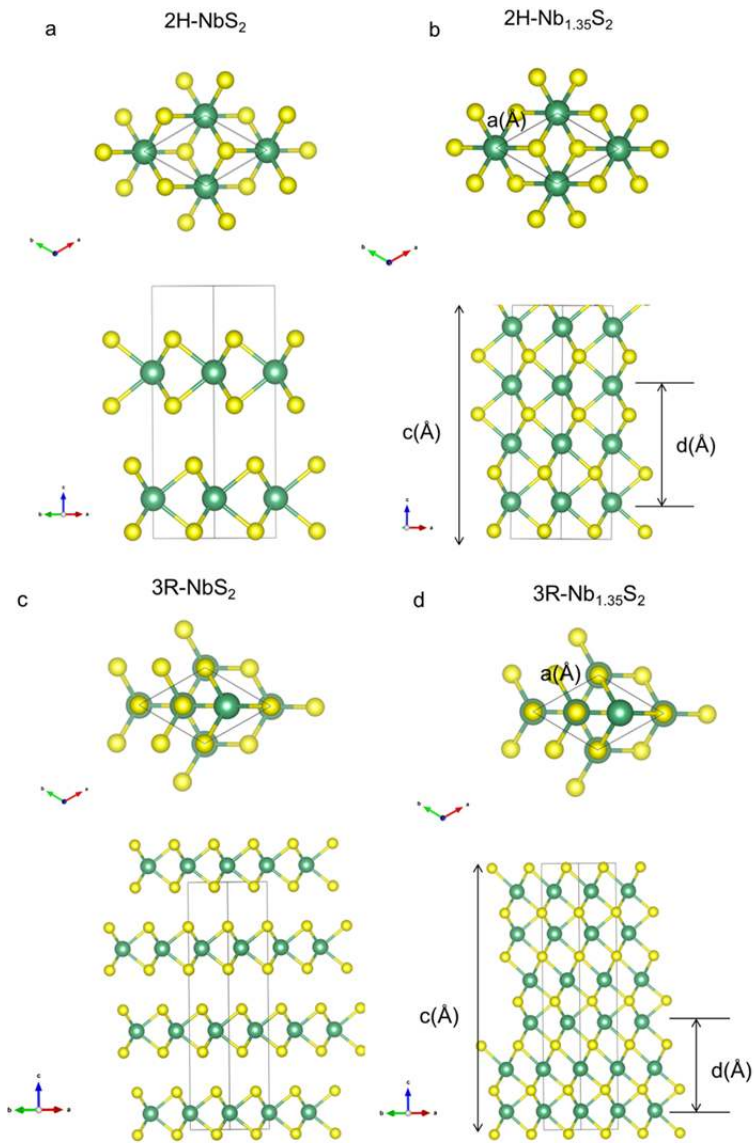
656

657 **Extended data Fig. 11 | Electrical properties of different NbS<sub>2</sub>.** **a**, I-V curve measured for the  
658 2H Nb<sub>1.35</sub>S<sub>2</sub> nanoflakes. The inset shows a SEM image of the device. An average value of 1800  
659 S/cm was obtained with the highest value being > 2400 S/cm. **b**, Comparison of conductivities  
660 for NbS<sub>2</sub>. NbS<sub>2</sub> is known as a metallic TMD material. However, the conductivity values in  
661 literature are scattered.<sup>30–33</sup>

662

663





664

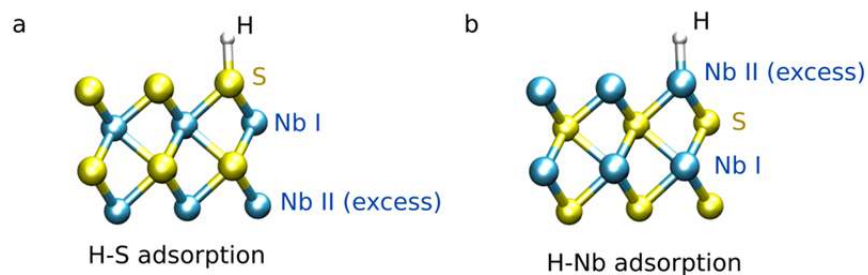
665

666

667

668 **Extended data Fig. 12** | Definition of geometrical parameters used at Extended Data Table 3 at  
 669 regular  $2\text{H-NbS}_2$  and  $3\text{R-NbS}_2$  phases as well as in the intercalated  $2\text{H-Nb}_{1.35}\text{S}_2$ ,  $3\text{R-Nb}_{1.35}\text{S}_2$   
 670 phases.

671



672  
673

674 **Extended data Fig. 13** | Definition of the geometry utilized to calculate the energetics of H at a  
675 monolayer NbS<sub>2</sub> with an additional Nb layer into the system. This would correspond to the  
676 smallest “intercalated phase” before it established in a 2H or 3R phases. The energetics for these  
677 systems are shown in Extended Data Table 7.

678

679

680 **Extended Data Table 1** | Comparison of TOF and exchange current density of TMDs catalysts

	$J_0$ ( $\mu\text{A}/\text{cm}^2$ )	$TOF$ at $J_0$	<i>ref</i>
2H-Nb <sub>1.35</sub> S <sub>2</sub>	800 ± 100	0.17s <sup>-1</sup> ± 0.03	Our work
2H-MoS <sub>2</sub> /Au	7.9	-	9
1T-WS <sub>2</sub>	20	0.043	3
2H-TaS <sub>2</sub>	100-179.47	-	5
Pt	450	0.9	9

681

682

683

**Extended Data Table 2** | Parameters used for synthesis of Nb<sub>1+x</sub>S<sub>2</sub>

	NbCl <sub>5</sub>	S	Temperature of NbCl <sub>5</sub>
3R-Nb <sub>1+x</sub> S <sub>2</sub>	35 mg	200 mg	300 °C
2H-Nb <sub>1+x</sub> S <sub>2</sub>	20 mg	100 mg	260 °C

684

685

686

687

688

689

690

691

692

693

694 **Extended Data Table 3 | Bulk lattice parameters using opt-B88 functional.** Simulations of  
 695 the geometrical parameters using opt-B88 functional including vdW interactions. Lattice  
 696 parameter,  $a(\text{\AA})$ , interlayer distance via Nb-Nb distance,  $d(\text{\AA})$ , and supercell length,  $c(\text{\AA})$  are  
 697 defined as in Extended Data Figure 12. Sound comparison with experimental data at different  
 698 phases is observed.

	2H-NbS <sub>2</sub>		3R-NbS <sub>2</sub>		2H-Nb <sub>1.35</sub> S <sub>2</sub>		3R-Nb <sub>1.35</sub> S <sub>2</sub>
	Theory	Exp.	Theory	Exp.	Theory	Exp.	Theory
$a(\square)$	3.34	3.31	3.35	3.33	3.31	3.306	3.24
$d(\square)$	5.97	5.91	6.05	5.98	6.64	6.35	6.81
$c(\square)$	11.935	11.89	18.17	17.81	13.29	12.6	20.43

699  
 700  
 701 **Extended Data Table 4 | Thermodynamic properties of S terminated surface using opt-B88**  
 702 **functional.** Energetics of the intercalated phase 2H-Nb<sub>1.35</sub>S<sub>2</sub> with adsorption of H at S atoms at  
 703 different coverages using opt-B88 functional. The large values of  $\Delta G_H$  (eV) at different  
 704 coverages rule out any HER using S-terminate surfaces.

Coverage	2H-Nb <sub>1.35</sub> S <sub>2</sub> (H-S adsorption)		
	0.11 ML	0.25 ML	1 ML
$\Delta E$ (eV)	1.011	0.804	1.459
ZPE (eV)	0.203	0.203	0.162
$\Delta G_H$ (eV)	1.245	1.077	1.694

705  
 706 **Extended Data Table 5 | Bulk lattice parameters using BEEF-vdW functional.** Simulations  
 707 of the geometrical parameters using BEEF-vdW functional including vdW interactions. Lattice  
 708 parameter,  $a(\text{\AA})$ , interlayer distance via Nb-Nb distance,  $d(\text{\AA})$ , and supercell length,  $c(\text{\AA})$  are  
 709 defined as in Extended Data Figure 12. Sound comparison with experimental data at different  
 710 phases is obtained.

	2H-NbS <sub>2</sub>		3R-NbS <sub>2</sub>		2H-Nb <sub>1.35</sub> S <sub>2</sub>		3R-Nb <sub>1.35</sub> S <sub>2</sub>
	Theory	Exp.	Theory	Exp.	Theory	Exp	Theory
$a(\square)$	3.35	3.31	3.35	3.33	3.30	3.30	3.22
$d(\square)$	6.34	5.91	6.36	5.98	6.65	6.35	6.65
$c(\square)$	12.67	11.89	19.10	17.81	13.30	12.6	19.94

712  
 713 **Extended Data Table 6 | Thermodynamic properties of S terminated surface using BEEF-**  
 714 **vdW functional.** Energetics of the intercalated phases  $2\text{H-Nb}_{1.35}\text{S}_2$  and  $3\text{R-Nb}_{1.35}\text{S}_2$  with  
 715 adsorption of H at S atoms at different coverages using BEEF-vdW functional. Similarly as in  
 716 the opt-B88 functional, the S-terminated surface seems inert for HER as long as H atoms bind on  
 717 S.

	2H-Nb <sub>1.35</sub> S <sub>2</sub> (H-S adsorption)			3R-Nb <sub>1.35</sub> S <sub>2</sub> (H-S adsorption)
Coverage	0.11 ML	0.25 ML	1 ML	0.25 ML
$\Delta E$ (eV)	1.005	0.766	1.41	0.619
ZPE (eV)	0.226	0.226	0.16	0.226
$\Delta G_{\text{H}}$ (eV)	1.302	0.989	1.64	0.915

718  
 719  
 720 **Extended Data Table 7 | Thermodynamic properties of a monolayer NbS<sub>2</sub> with additional**  
 721 **Nb atoms in the structure.** Energetics of the monolayer NbS<sub>2</sub> with additional Nb atoms  
 722 incorporated into the structure (see Extended Data Fig. 13). This system corresponds to the  
 723 smallest situation where the effect of additional Nb atoms could be appreciated on the free  
 724 energies and HER of monolayer NbS<sub>2</sub>. The adsorption of H is simulated either at S-terminated  
 725 the surface or at Nb-terminated. The large variations in energy between both configurations  
 726 indicate the H adatoms would prefer binding at the Nb sites rather than on S. This suggests that  
 727 additional Nb atoms have a strong effect on the chemical kinetics of the reaction changing the  
 728 preferable site of H adsorption for efficient HER. Similar results as those in Ref. 22 are  
 729 compared for the monolayer NbS<sub>2</sub> without additional Nb atoms. Calculations at the level of  
 730 BEEF-vdW functional.

	Monolayer NbS <sub>2</sub>	Monolayer NbS <sub>2</sub> Nb terminated (H-S adsorption)	Monolayer NbS <sub>2</sub> Nb terminated (H-Nb adsorption)
Coverage	0.0625 ML	0.25 ML	0.25 ML
$\Delta E$ (eV)	-0.185	1.039	0.072
ZPE (eV)	0.226	0.215	0.098
$\Delta G_{\text{H}}$ (eV)	0.11	1.324	0.24

731

732  
733  
734  
735  
736  
737  
738

**Extended Data Table 8 | Thermodynamic properties of Nb terminated slab with adsorption of H on Nb atoms.** Energetics of the intercalated phases 2H-Nb<sub>1.35</sub>S<sub>2</sub> and 3R-Nb<sub>1.35</sub>S<sub>2</sub> with adsorption of H on Nb atoms using BEEF-vdW functional. The resulting geometries are those shown in Figure 4. The comparison between 2H-Nb<sub>1.35</sub>S<sub>2</sub> and 3R-Nb<sub>1.35</sub>S<sub>2</sub> clearly indicates that the former would give better HER results than the latter, as it follows closely the measurements.

	2H-Nb <sub>1.35</sub> S <sub>2</sub> (Nb Terminated)	3R-Nb <sub>1.35</sub> S <sub>2</sub> (Nb Terminated)
Coverage	0.25 ML	0.25 ML
$\Delta E$ (eV)	-0.056	0.066
ZPE (eV)	0.099	0.098
$\Delta G_H$ (eV)	0.11	0.235

739  
740  
741

- 742 28. Li, S. *et al.* Halide-assisted atmospheric pressure growth of large WSe<sub>2</sub> and WS<sub>2</sub>  
743 monolayer crystals. *Appl. Mater. Today* **1**, 60–66 (2015).
- 744 29. Suh, J. *et al.* Doping against the Native Propensity of MoS<sub>2</sub>: Degenerate Hole Doping by  
745 Cation Substitution. *Nano Lett.* **14**, 6976–6982 (2014).
- 746 30. Huang, Y. H., Peng, C. C., Chen, R. S., Huang, Y. S. & Ho, C. H. Transport properties in  
747 semiconducting NbS<sub>2</sub> nanoflakes. *Appl. Phys. Lett.* **105**, 93106 (2014).
- 748 31. Molenda, J., Bak, T. & Marzec, J. Electrical and electrochemical properties of niobium  
749 disulphide. *Phys. Status Solidi A* **156**, 159–168 (1996).
- 750 32. Niazi, A. & Rastogi, A. K. Low-temperature resistance minimum in non-superconducting  
751 3R-Nb<sub>1+x</sub>S<sub>2</sub> and 3R-Ga<sub>x</sub>NbS<sub>2</sub>. *J. Phys. Condens. Matter* **13**, 6787 (2001).
- 752 33. Zhao, S. *et al.* Two-dimensional metallic NbS<sub>2</sub>: growth, optical identification and  
753 transport properties. *2D Mater.* **3**, 25027 (2016).

- 754 34. Kresse, G. & Hafner, J. Ab initio molecular dynamics for liquid metals. *Phys. Rev. B* **47**,  
755 558–561 (1993).
- 756 35. Kresse, G. & Hafner, J. Ab initio molecular-dynamics simulation of the liquid-  
757 metal\char21 {}amorphous-semiconductor transition in germanium. *Phys. Rev. B* **49**, 14251–  
758 14269 (1994).
- 759 36. Kresse, G. & Furthmüller, J. Efficiency of ab-initio total energy calculations for metals  
760 and semiconductors using a plane-wave basis set. *Comput. Mater. Sci.* **6**, 15–50 (1996).
- 761 37. Kresse, G. & Furthmüller, J. Efficient iterative schemes for ab initio total-energy  
762 calculations using a plane-wave basis set. *Phys. Rev. B* **54**, 11169–11186 (1996).
- 763 38. Klimeš, J., Bowler, D. R. & Michaelides, A. Chemical accuracy for the van der Waals  
764 density functional. *J. Phys. Condens. Matter* **22**, 22201 (2010).
- 765 39. Wellendorff, J. *et al.* Density functionals for surface science: Exchange-correlation model  
766 development with Bayesian error estimation. *Phys. Rev. B* **85**, 235149 (2012).
- 767 40. Monkhorst, H. J. & Pack, J. D. Special points for Brillouin-zone integrations. *Phys. Rev.*  
768 *B* **13**, 5188–5192 (1976).
- 769
- 770
- 771